Pneumococcal H_2O_2 Reshapes Mitochondrial Function and Reprograms Host Cell Metabolism

Anna Scasny[1], Babek Alibayov[1], Ngoc Hoang[2], Ana G. Jop Vidal[1], Kenichi Takeshita[1], Eva Bengten[1,3], Antonino Baez[1,4], Wei Li[5], Jonathan Hosler[1], Kurt Warncke[5], Kristin Edwards[2], Jorge E. Vidal[1,3]

[1]Department of Cell and Molecular Biology, [2]Department of Pharmacology and Toxicology, [3]Center for Immunology and Microbial Research, School of Medicine, University of Mississippi Medical Center, Jackson, MS; [4]Centro de Investigaciones en Ciencias Microbiológicas (CICM), Instituto de Ciencias (IC), Benemérita Universidad Autónoma de Puebla (BUAP), Puebla, México; [5]Department of Physics, Emory University, Atlanta GA

Running title: Spn-H_2O_2 drives metabolic reprograming

#Address correspondence to:
Jorge E. Vidal, PhD
2500 North State Street, Jackson Mississippi 39216
Phone: (601) 984-1711, Fax: (601) 984-1708
Email jvidal@umc.edu,

Summary

Streptococcus pneumoniae (Spn) is a primary cause of pneumonia, induces acute lung parenchymal infection, damaging through a unique metabolic pathway that generates hydrogen peroxide (H_2O_2) as a byproduct. This study reveals that Spn-derived H_2O_2, primarily produced by pyruvate oxidase (SpxB), inhibits the tricarboxylic acid (TCA) cycle in lung epithelial cells by targeting aconitase, glutamate dehydrogenase, and α-ketoglutarate dehydrogenase. This inhibition leads to citrate accumulation and reduced NADH production for oxidative phosphorylation, while RNA sequencing shows SpxB-dependent upregulation of glycolytic genes (e.g., HK2, PFKP), limiting pyruvate entry into the TCA cycle. Consequently, glucose consumption and lactate/acetate production increase, resembling a Warburg-like metabolic shift that supports bacterial survival. Despite TCA cycle suppression, mitochondrial membrane potential remains largely unaffected, with minimal apoptosis induced by Spn-mediated stress. These findings elucidate a novel mechanism by which Spn manipulates host metabolism to facilitate infection, highlighting potential therapeutic targets for pneumococcal diseases.

Highlights

- Spn-derived SpxB-generated H_2O_2 directly inhibits TCA cycle enzymes ACO2, GDH, and OGDHC.
- Spn-H_2O_2 disrupts mitochondrial respiration, increases citrate levels, and enhances glucose consumption with elevated lactate and acetate production.
- SpxB-dependent H_2O_2 induces transcriptional dysregulation, upregulating HK2 and PFKP while reducing pyruvate entry into the TCA cycle.
- H_2O_2-mediated reprogramming shifts host cells to a Warburg-like metabolic phenotype.
- Spn-H_2O_2 triggers limited apoptosis and maintains mitochondrial membrane potential, supporting bacterial survival.

Graphical abstract

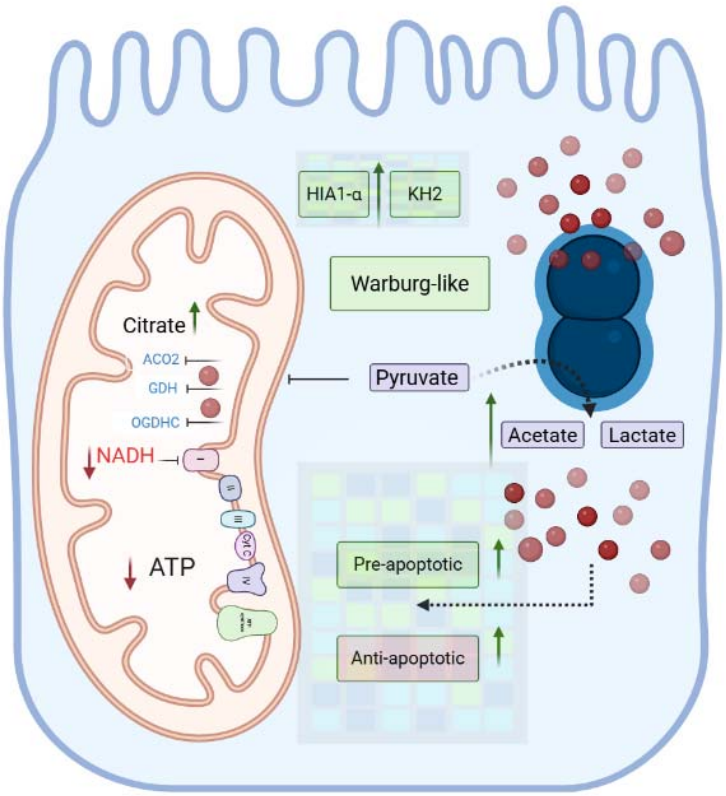

Introduction.

Streptococcus pneumoniae (Spn), commonly known as the pneumococcus, is a major global health burden, particularly among children and the elderly, causing significant morbidity and mortality through pneumonia and other invasive pneumococcal diseases (IPDs)[1,2]. During pneumococcal pneumonia, lung colonization induces profound cellular damage, disrupting critical structural components such as ciliary function, β-actin architecture, and nuclear and mitochondrial DNA[3-5]. Despite progress in understanding pneumococcal pathogenesis, the mechanisms driving host cell death and tissue injury remain incompletely elucidated.

A hallmark of Spn pathogenesis is its efficient metabolic activity, primarily driven by glycolysis, which supports energy and biomass production through glucose catabolism. A critical byproduct, hydrogen peroxide (H_2O_2), a reactive oxygen species, is increasingly implicated in host cell damage[1,6]. Spn produces H_2O_2 continuously via glycolysis, its primary ATP-generating pathway, with some strains generating up to 2 mM H_2O_2, detectable extracellularly and intracellularly[7-9]. Pyruvate oxidase (SpxB) and lactate oxidase (LctO) primarily drive H_2O_2 production, with SpxB converting pyruvate to acetyl phosphate and LctO oxidizing lactate to pyruvate, both yielding H_2O_2 alongside ATP[9,10]. SpxB accounts for ~85% of total H_2O_2 production in Spn, while LctO contributes ~15%, reflecting adaptations to oxygen-rich environments like the lungs[9,10].

Substantial evidence implicates Spn-derived H_2O_2 (hereafter Spn-H_2O_2) in host cell death and disease severity in animal models[11-16]. Our previous studies have shown that Spn-H_2O_2 inhibits *ex vivo* Complex I-driven respiration[17]. Additionally, Spn infection induces mitochondrial DNA leakage in lung cells, triggering a type I interferon response[18], and in an aged murine model of pneumonia, it dysregulates mitochondrial complex expression, elevates

oxidative stress, and impairs antioxidant defenses, leading to reduced ATP production[19]. These findings underscore the role of H_2O_2 in disrupting mitochondrial function, exacerbating cytotoxicity. Furthermore, Spn alters host cell nutrient availability by depleting epithelial glycans and enhancing macrophage glutamine uptake, thereby increasing bacterial access to host-derived carbohydrates and amino acids during infection[20]. These metabolic shifts fuel bacterial proliferation and inflammation, driving disease progression. Concurrently, Spn infection activates both apoptosis and pyroptosis, indicating complex cytotoxic mechanisms[3,4,21,22]. Our recent studies reveal that Spn-H_2O_2 disrupts actin and tubulin cytoskeletons in bronchial and alveolar epithelial cells, impairing structural stability and protein trafficking, leading to microtubule catastrophe and cell swelling due to loss of actin stress fibers[17,23]. This mirrors cytoskeletal damage in ventricular cardiomyocytes exposed to 100 μM H_2O_2, where oxidation of specific cysteine residues (Cys213, Cys295, and Cys305 in α-globin; Cys129 in β-globin) disrupts tubulin interactions, inhibiting microtubule polymerization[24-26]. Moreover, Spn-H_2O_2 oxidizes hemoglobin *in vitro* and *in vivo*, inducing aggregation via crosslinking of α- and β-globin chains[27,28] and generating MetOH, a product of methionine-55 oxidation in the β-chain linked to globin collapse[23].

Mitochondria are essential for many cellular functions, with two of its main functions being to produce ATP through oxidative phosphorylation (OxPhos) and regulate programmed cell death[29]. The TCA cycle, a central metabolic pathway, supplies essential intermediates such as NADH and $FADH_2$ to the electron transport chain (ETC) for ATP synthesis[30]. In this process, exergonic electron transfer to O_2 is coupled to the endergonic phosphorylation of ADP to ATP via four ETC complexes (I–IV), which contain heme- or iron-sulfur (Fe-S)-containing proteins[31,32]. For instance, Complexes I and III include Fe-S proteins, while Complexes II, III,

and IV incorporate hemoproteins with hemes b, c, and a, respectively; cytochrome c (Cyt*c*) also carries heme c[31,33]. We have previously demonstrated that Spn-H_2O_2 oxidizes Cytc[17,34], and this oxidant is produced intracellularly during pneumococcal invasion of lung cells[23], highlighting a direct mechanism of mitochondrial disruption.

To establish infection, Spn invades bronchial and alveolar epithelial cells, adapting to the intracellular environment for survival and proliferation. Spn's metabolic configuration resembles that of mitochondria under stress conditions (e.g., hypoxia), with an incomplete TCA cycle lacking α-ketoglutarate dehydrogenase, which converts α-ketoglutarate to succinyl-CoA, forcing reliance on glycolysis for energy production in resource-limited niches[35,36]. Similarly, Spn possesses a partial electron transport chain (ETC), missing NADH:quinone oxidoreductase (Complex I) and cytochrome bc1 complex (Complex III), but encoding a truncated succinate dehydrogenase (Complex II) for fumarate reduction, a cytochrome bd oxidase (Complex IV) for oxygen detoxification, and an ATP synthase (Complex V) likely for proton homeostasis. This configuration, while suited for oxygen-limited environments, mirrors mitochondrial ETC reliance on cytochrome oxidases but results in continuous H_2O_2 production, amplifying oxidative stress in host cells. The absence of a robust TCA cycle and ETC also impairs Spn's ability to detoxify reactive oxygen species, exacerbating host cell damage. Furthermore, Spn exploits host resources by scavenging metabolites such as amino acids and carbohydrates, upregulating glutamine uptake and depleting epithelial glycans to fuel its metabolism and enhance virulence[20]. These metabolic adaptations highlight Spn's ability to disrupt host cellular processes through strategic reprogramming, motivating this study to investigate the H_2O_2-mediated effects on host mitochondrial function and metabolism during pneumococcal infection.

RESULTS

Oxidation of Cyt*c* by *S. pneumoniae*-H_2O_2 creates a tyrosyl radical. Spn-H_2O_2 is known to oxidize heme groups in hemoglobin and Cyt*c*, key components of the mitochondrial ETC[17,23,34]. To investigate the kinetics of H_2O_2-mediated Cyt*c* oxidation, Todd-Hewitt broth supplemented with yeast extract (THY) was enriched with 56 µM Cytc (THY-Cyt*c*) and infected with Spn. Supernatants from time-course experiments were analyzed by spectroscopic methods to assess oxidation dynamics[37,38]. Compared to mock-infected THY-Cyt*c* cultures, statistically significant heme degradation was observed in those incubated with TIGR4 for 6 h (Fig. 1A) and in those infected with EF3030 and incubated for 4 and 6 h (Fig. 1C). In mock-infected THY-Cyt*c* cultures incubated for up to 6 h, the Soret peak of heme-Fe^{3+} exhibited a maximum absorbance at 405 nm (Fig. 1B and 1D). In contrast, heme degradation observed in cultures of Spn strains, TIGR4 (Fig. 1B) or EF3030 (Fig. 1D) was characterized by the significant loss of the Soret peak and the appearance of a different species absorbing at 325 nm (Fig. 1B and 1D, arrow). Heme degradation and the formation of the 305 nm species were not detected in cultures of wt strains treated with catalase or in cultures of strains deficient in Spn-H_2O_2 production such as TIGR4Δ*spxB*Δ*lctO* or EF3030Δ*spxB*Δ*lctO* (Fig. 1B and 1D).

The α and β absorption peaks of Cyt*c*, obserbed at 550 and 520 nm, respectively[39,40] underwent oxidation in 6 h cultures of TIGR4 (Fig. 1E) and EF3030 (Fig. 1F) indicative of porphyrin ring degradation. Notably, TIGR4Δ*spxB*Δ*lctO* retained residual oxidative activity on the α and β peaks, possibly via minor SpxB/LctO-independent pathways. This residual activity was completely abrogated upon catalase treatment (data not shown), underscoring the role of H_2O_2 in driving heme degradation in these strains.

Previous studies have shown that H_2O_2 oxidation of hemoproteins generates highly reactive and toxic radicals, including the ferryl radical ($^{\bullet}Hb^{4+}$), and tyrosyl radical[5,41-44]. To determine whether radical species form during Cyt*c* oxidation by Spn-derived H_2O_2, pneumococcal strains TIGR4, EF3030, their Δ*spxB*Δ*lctO* mutants, and a complemented strain (ΩspxBΩlctO) were cultured in Todd-Hewitt broth with yeast extract (THY) medium. Supernatants were combined with Cyt*c* and the spin trap DEPMPO [5-(Diethoxyphosphoryl)-5-methyl-1-pyrroline-N-oxide, 98%], and radical formation was monitored using continuous wave electron paramagnetic resonance (EPR). EPR spectra from TIGR4, TIGR4ΩspxBΩlctO, and EF3030 supernatants with Cyt*c* were identical (Fig. 1G), indicating tyrosyl radical formation from Cyt*c* oxidation. No EPR signal was detected in Δ*spxB*Δ*lctO* mutant supernatants or wild-type cultures treated with catalase. The observed EPR spectra are consistent with both protein-attached and free-solution carbon-centered radicals.

***S. pneumoniae*-derived H_2O_2 contributes to mitochondrial aggregation and apical migration within alveolar cells.** Disruption of cytochrome c (Cytc) increases reactive oxygen species (ROS) production and triggers apoptotic cell death, which can induce mitochondrial morphological changes through fusion or fission events, altering organelle structure by combining or dividing mitochondria, respectively[45]. To investigate the impact of Spn infection on mitochondrial structure, human alveolar A549 cells were infected with pneumococcal strains TIGR4, EF3030, and their Δ*spxB*Δ*lctO* mutants for 8 h. Cells were stained for mitochondria (green), DNA (blue), and actin (red), and analyzed by confocal microscopy (Fig. 2).

In mock-infected control A549 cells, mitochondria exhibited a well-developed, interconnected network of elongated, filamentous structures surrounding the nuclei,

168 characteristic of healthy, actively respiring cells (Fig. 2A). In contrast, both TIGR4-, and
169 TIGR4Δ*spxB*Δ*lctO*-infected alveolar cells displayed fragmented and punctate mitochondria
170 with a diffuse cytoplasmic distribution. These mitochondria were significantly smaller than
171 those in mock-infected cells and exhibited irregular morphologies (Fig. 2A).

172 At different magnifications, A549 cells infected with Spn wild-type strains TIGR4 or
173 EF3030 exhibited rounding and aggregation, with clusters of mitochondria forming around the
174 nuclei (Fig. 2B, arrows). A more pronounced aggregation of mitochondria was apparent in
175 EF3030-infected cells (Fig. 2B, arrows). Three-dimensional imaging analysis revealed that
176 these mitochondrial clusters were predominantly localized on the apical surface of the infected
177 cells (Fig. 2B and 2C). In contrast, mitochondria in TIGR4Δ*spxB*Δ*lctO*- and
178 EF3030Δ*spxB*Δ*lctO*-infected alveolar cells appeared unevenly distributed, with varying sizes
179 and intensities, suggesting aggregation around certain areas, near the nuclei or in regions of
180 cellular stress (Fig. 2B and 2C).

181 Employing three-dimensional analysis, we categorized mitochondria in mock-infected
182 and Spn-infected cells based on their spatial proximity to the apical surface. Mitochondria
183 located within 5 µm of the cell surface were classified as 'apical,' while those positioned deeper
184 within the cellular architecture were designated as 'middle-bottom' (Fig. 2D). Quantitative
185 assessment revealed that the area of mitochondrial aggregates at the apical side of TIGR4-
186 and EF3030-infected alveolar epithelial cells (Fig. 2E) was significantly greater than that
187 observed in mock-infected cells or cells infected with hydrogen peroxide-deficient knockout
188 mutants (Fig. 2F and 2G), highlighting the impact of Spn-derived H_2O_2 on mitochondrial
189 clustering and distribution. Taken together, these results indicate that Spn-derived H_2O_2

induces mitochondrial aggregation and apical migration in infected alveolar cells, likely exacerbating oxidative stress and apoptosis by disrupting mitochondrial dynamics.

***S. pneumoniae* inhibits mitochondrial respiration in host cells.** To investigate the impact of Spn-H_2O_2 on mitochondrial respiration, we employed an *ex vivo* model of infection. Rat heart mitochondria were isolated and subsequently incubated with supernatants from TIGR4, EF3030, or its H_2O_2-deficient mutant, Δ*spxB*Δ*lctO*, following 4 hours of growth in THY. Hydrogen peroxide levels in the supernatants were quantified. Strain TIGR4 produced a median H_2O_2 concentration of 499.5 µM, while EF3030 secreted 1119 µM H_2O_2 into the supernatant (Fig. 3A). The H_2O_2 levels in the supernatants of the mutants derivatives were significantly lower (<8.86 µM) (Fig. 3A).

Oxygen consumption, a proxy for electron transference through complex-I (CIDR), or complex-II (CIIDR), driven respiration (Fig. 3B), was investigated using a high-resolution Oroboros O2k FluoRespirometer. Isolated mitochondria were treated with the TCA cycle substrates glutamate and malate to generate NADH and initiate CIDR, which facilitates the transfer of electrons through complexes I, III, and IV (Fig. 3B). Alternatively, mitochondria were treated with succinate to generate $FADH_2$ and drive electron transfer through CIIDR[29,33] (Fig. 3B). Notably, mitochondrial CIDR was significantly inhibited by supernatants from TIGR4 at 5 µM H_2O_2, with maximal inhibition of mitochondrial respiration was observed at concentrations ≥12.5 µM (Fig. 3C). In contrast, CIIDR was not inhibited by TIGR4 cultures containing the lowest H_2O_2 concentration, but statistically significant inhibition occurred at concentrations ≥25 µM (Fig. 3D). The factor in the supernatant causing the inhibition of mitochondrial respiration was Spn-H_2O_2, as an equivalent volume of supernatant from the TIGR4Δ*spxB*Δ*lctO* mutant did

not inhibit CIDR, whereas the supernatant from the complemented strain caused CIDR inhibition (Fig. 3E). A comparison of residual CIDR and CIIDR activity revealed a marked difference between mock-infected and TIGR4-treated mitochondria. Mitochondria exposed to TIGR4 cultures exhibited only 10% of the CIDR activity observed in the mock-infected control, while CIIDR activity remained significantly higher (Fig. 3F). These findings suggest that supernatant from Spn strain TIGR4, containing H_2O_2, inhibits cellular respiration by targeting components of the mitochondrial complex I, the NADH dehydrogenase complex, or enzymes of the TCA cycle responsible for synthesizing the electron donor NADH.

***Streptococcus pneumoniae*-mediated inhibition of mitochondrial respiration occurs independently of electron transport chain activity.** To further investigate the impact of Spn on mitochondrial function, we assessed the oxidative activity of individual complexes within the electron transport chain (ETC). This was achieved by measuring the activity of each complex in mitochondria exposed to either sterile bacterial culture medium (mock) or supernatants from Spn strains TIGR4 and EF3030, as outlined in the Materials and Methods section. Notably, no significant differences were observed in the oxidative capacity of complex I for its substrate NADH (Fig. 3G), or in the activity of any other ETC complexes, between mitochondria exposed to bacterial culture medium and those exposed to Spn supernatants (Fig. S1A-C). Therefore, inhibition of mitochondrial respiration by Spn occurs upstream the ETC.

***S. pneumoniae* H_2O_2-mediated inhibition of TCA cycle enzymes downstream of malate dehydrogenase in mitochondrial respiration.** Given that NADH, the substrate for complex I, can be oxidized in the presence of Spn cultures, yet these cultures inhibit respiration when

236 TCA cycle substrates (generating NADH) are supplemented, we hypothesized that Spn
237 cultures specifically oxidize enzymes within the TCA cycle. To assess this, we stimulated
238 cellular oxygen consumption in CIDR with a panel of TCA cycle substrate mixtures: pyruvate
239 and malate, glutamate and malate, or succinate alone (Fig. 4A). It is well stablished that the
240 addition of co-substrates enhances OxPhos capacity by shuttling electrons through complex
241 I[46]. Mitochondrial respiration driven by substrates pyruvate and malate was not significantly
242 inhibited by cultures of Spn (Fig. 4B). Similarly, cellular oxygen consumption stimulated by
243 incubation with succinate (via complex II) was unaffected by cultures of the pneumococcus.
244 Conversely, Spn strains TIGR4 and EF3030 significantly inhibited mitochondrial respiration
245 induced by glutamate and malate (Fig. 4B). This data supports the hypothesis that Spn
246 cultures inhibit enzymes of the TCA cycle, specifically downstream of citrate synthase (CS),
247 which catalyzes the irreversible conversion of acetyl-CoA and oxaloacetate to citrate.

248 β-oxidation of medium-chain and long-chain fatty acids in the mitochondrial matrix
249 produces acetyl-CoA, which reacts with oxaloacetate to form citrate in the TCA cycle. We
250 assessed whether supplementing oleate (long-chain) or octanoate (medium-chain) to isolated
251 mitochondria incubated with Spn cultures inhibits CIDR. Compared to the mock control,
252 cultures of both strains significantly inhibited CIDR (Fig. 4C), further indicating that the
253 inhibition induced by Spn cultures occurs at or downstream of CS.

254 In the mitochondria, aconitase (ACO2) is located downstream of CS and catalyzes the
255 reversible isomerization of citrate to isocitrate. The resulting isocitrate is then decarboxylated
256 to α-ketoglutarate by isocitrate dehydrogenase 3 (IDH3) (Fig. 4A). Glutamate in the
257 mitochondria is converted to α-ketoglutarate by glutamate dehydrogenase (GDH), which is
258 then decarboxylated to succinyl-CoA by α-ketoglutarate dehydrogenase (OGDHC) (Fig. 4A).

We assessed the activity of ACO2, GDH, and OGDHC in isolated mitochondria exposed to cultures of Spn wt strains producing H_2O_2, comparing them to mock-infected conditions and to cultures of Δ*spxB*Δ*lctO* mutants. Both TIGR4 and EF3030, caused a significant inhibition of the enzymatic activity of ACO2 (Fig. 4D), GDH (Fig. 4E), and OGDHC (Fig. 4F), compared to mock-infected cultures or cultures of isogenic Δ*spxB*Δ*lctO* mutants. To further validate these findings in a host cell model, we measured GDH activity in Calu-3 bronchial epithelial cells, either mock-infected or infected with Spn. Consistent with the *ex vivo* data, GDH activity in TIGR4-infected Calu-3 cells was significantly reduced compared to mock-infected controls or cells infected with Δ*spxB*Δ*lctO* (Fig. 4G), supporting the notion that Spn-H_2O_2 directly inhibits GDH in lung epithelial cells, contributing to TCA cycle disruption and subsequent metabolic reprogramming.

Spn-mediated transcriptional regulation of mitochondrial genes in lung cells. RNA sequencing (RNAseq) analysis of bronchial Calu-3 cells, a differentiated lung epithelial model derived from adenocarcinoma, revealed extensive transcriptional reprogramming following infection with TIGR4. Compared to mock-infected controls, TIGR4 infection dysregulated 2,684 genes dysregulated (FDR <0.05, log2 fold change >0.5), a response largely driven by SpxB, as infection with the isogenic TIGR4Δ*spxB* mutant dysregulated only 163 genes (Fig. 2SA and 2SB). Gene ontology (GO) analysis indicated that TIGR4 infection induces a broad stress response, with significant enrichment of pathways related to DNA damage response, cell cycle regulation, and mitochondrial function (Fig. 2SC and 2SC). In contrast, TIGR4Δ*spxB* infection elicited a narrower response, primarily involving NF-κB signaling and apoptosis pathways. Notably, TIGR4 infection dysregulated 237 mitochondrial-related genes (GO:0005739),

compared to 19 in TIGR4Δ*spxB*-infected cells, highlighting SpxB's critical role in mitochondrial gene regulation (Suppl. Table S1). Calu-3 cells, exhibiting a metabolic profile less dependent on Warburg metabolism than more aggressive cancer cell lines, provide a physiologically relevant model for studying epithelial responses to bacterial infection[47].

Among the dysregulated genes, TIGR4 infection significantly upregulated IDH3 (isocitrate dehydrogenase 3) and PDK1 (pyruvate dehydrogenase kinase 1) in Calu-3 cells (Fig. S4H), while downregulating PC (pyruvate carboxylase), PDK2 (pyruvate dehydrogenase kinase 2), and PDPR (pyruvate dehydrogenase phosphatase regulatory subunit). These genes regulate the pyruvate dehydrogenase complex (PDC), which controls pyruvate entry into the mitochondrial TCA cycle. Upregulation of PDK1 likely inhibits PDC activity, while concurrent downregulation of PDK2 and PDPR further suppresses PDC function, potentially limiting mitochondrial oxidative phosphorylation and mitigating oxidative stress. This pattern was absent in TIGR4Δ*spxB*-infected cells, which lack pyruvate oxidase and H_2O_2 production. However, a similar dysregulation was observed with the H_2O_2-producing TIGR4Δ*lctO* mutant (Fig. 44H), emphasizing SpxB-mediated oxidative stress in driving these changes.

Supporting SpxB-driven transcriptional reprogramming, genes encoding oxidative stress response enzymes, including SOD2 (superoxide dismutase 2), TXNRD1 (thioredoxin reductase 1), HMOX1 (heme oxygenase 1), and NFKB1 (nuclear factor kappa B subunit 1), were upregulated in Calu-3 cells infected with TIGR4 and TIGR4Δ*lctO* (Fig. 4I). Expression remained unchanged in TIGR4Δ*spxB*-infected cells, highlighting SpxB's role in eliciting a robust antioxidant defense. Similar dysregulation of PDK1 and SOD genes was observed in non-cancerous bronchial BEAS-2B cells infected with Spn strain D39[48] (Fig. 7E).

Spn-H_2O_2-driven metabolic reprogramming in lung epithelial cells. Inhibition of key TCA cycle enzymes, including ACO2, GDH, and OGDHC, by Spn (Spn) may lead to citrate accumulation in host cells. To investigate, intracellular and extracellular citrate concentrations were measured in mock-infected Calu-3 bronchial epithelial cells and compared to cells infected with Spn strains TIGR4 or TIGR4Δ*spxB*Δ*lctO* for 8 h. Extracellular citrate levels, quantified by high-performance liquid chromatography (HPLC), were significantly elevated in TIGR4- and TIGR4Δ*spxB*Δ*lctO*-infected cells (median 227 µM and 441 µM, respectively) compared to mock-infected controls (4.04 µM) (Fig. 5A). Although Spn lacks a complete TCA cycle, it encodes a citrate synthase homolog, gltA (SP0918)[36]. Citrate levels in Spn culture supernatants (without host cells) were comparable between TIGR4 and TIGR4Δ*spxB*Δ*lctO*, suggesting bacterial contribution to extracellular citrate (Fig. 5A). However, intracellular citrate concentrations were significantly higher in TIGR4-infected cells compared to mock-infected or TIGR4Δ*spxB*Δ*lctO*-infected cells, indicating that H_2O_2-producing Spn exacerbates mitochondrial citrate accumulation, likely due to TCA cycle inhibition.

Metabolite analysis revealed that Spn infection enhances glucose consumption. Baseline glucose in Calu-3 cells was 1.8 g/L, decreasing to 1.2 g/L in mock-infected cells after 8 h. In TIGR4- and TIGR4Δ*spxB*Δ*lctO*-infected cells, glucose levels dropped below 0.16 g/L (Fig. 5C), while Spn cultures alone consumed less than 0.65 g/L, indicating a host-specific response likely driven by SpxB-mediated oxidative stress and TCA cycle suppression. Acetate production, absent in mock-infected cells, increased to 4.54 mM in TIGR4-infected cells but was lower in TIGR4Δ*spxB*Δ*lctO*-infected cells (1.58 mM) (Fig. 5E). Spn cultured alone produced 2.35 mM (TIGR4) and 0.29 mM (TIGR4Δ*spxB*Δ*lctO*) acetate, reflecting SpxB's role in acetate synthesis via acetyl phosphate under aerobic conditions (Fig. 5D). Lactate levels

further highlighted metabolic shifts. Extracellular lactate in mock-infected cells was 1.96 mM, increasing to 8.9 mM (TIGR4) and 8.4 mM (TIGR4Δ*spxB*Δ*lctO*) in infected cells, with Spn alone producing 4.7 mM (TIGR4) and 6.3 mM (TIGR4ΔspxBΔlctO) (Fig. 5F). Intracellular lactate, 1.17 mM in mock-infected cells, decreased significantly in infected cells, likely due to Spn-induced cytotoxicity (Fig. 5G). RNA-seq analysis revealed significant upregulation of glycolysis-related genes in TIGR4-infected cells, including IER3, DDIT4, HK2, HIF1A, and PFKP ($\log_2$ fold change 1–4, FDR <0.05), with HK2 and PFKP also upregulated in TIGR4Δ*lctO*-infected cells (Fig. 5H, 5I). In TIGR4Δ*spxB*Δ*lctO*-infected cells, most genes were unchanged except for HK2, BPGM, and HIF1A, underscoring SpxB-H_2O_2's role in glycolytic reprogramming.

Collectively, Spn-H_2O_2 induces profound metabolic reprogramming in Calu-3 cells, marked by citrate accumulation, enhanced glucose consumption, increased extracellular lactate and acetate, and selective upregulation of glycolytic genes, reflecting a host response to SpxB-mediated mitochondrial impairment.

Infection with *S. pneumoniae* does not cause loss of alveolar mitochondrial membrane potential. Increased permeability of the mitochondrial inner membrane (IMM) can dissipate the proton electrochemical gradient and destabilize ΔΨm, both of which are essential for ATP synthesis via ATP synthase. Given that Spn-H_2O_2 inhibit the TCA cycle, we hypothesized that enhanced mitochondrial permeability contributes to this effect. To test this, ΔΨm—established primarily by proton translocation through complexes I, III, and IV of the electron transport chain (ETC)—was assessed, as it, together with the proton gradient, constitutes the proton-motive force driving ATP production[49]. In healthy mitochondria, ΔΨm is tightly regulated; its dissipation or reduction signals impaired ATP synthesis, mitochondrial dysfunction, and increased reactive

oxygen species (ROS) production. Here, we evaluated the impact of Spn-derived H_2O_2 on ΔΨm in A549 alveolar epithelial cells using flow cytometry with the potentiometric dye JC-1. across the IMM that drives ATP production via ATP synthase.

In cells with intact mitochondrial function, the cell-permeant dye JC-1 accumulates in polarized mitochondria, forming aggregates that exhibit a balanced fluorescence emission profile, with an approximately equal ratio of Texas Red (~590 nm) to FITC (~530 nm). This dual-emission state is detected as a +Texas Red/+FITC double-positive population in flow cytometry, indicative of robust ΔΨm. Consistent with this, uninfected A549 cells stained with JC-1 displayed this characteristic pattern, reflecting maintained ΔΨm (Fig. 6A). In contrast, treatment with carbonyl cyanide m-chlorophenyl hydrazone (CCCP), a known ΔΨm uncoupler, induced complete depolarization, shifting the population to -Texas Red/+FITC single-positive cells (Fig. 6B).

To assess the effects of Spn-derived H_2O_2 on mitochondrial function, A549 cells were infected with wild-type strains TIGR4 and EF3030, or their respective H_2O_2-deficient mutants TIGR4Δ*spxB*Δ*lctO* and EF3030Δ*spxB*Δ*lctO*. Mitochondrial membrane potential (ΔΨm) was then quantified using JC-1 staining and flow cytometry. Relative to the CCCP-treated positive control, which induces complete ΔΨm dissipation by enhancing proton permeability across the IMM, infections with TIGR4 and EF3030 resulted in significantly less mitochondrial depolarization (Figs. 6D, 6G, 6I). Similarly, treatment of A549 cells with 2 mM H_2O_2 alone did not alter ΔΨm (Fig. 6D), suggesting that H_2O_2 at this concentration does not directly impair mitochondrial membrane integrity. Furthermore, A549 cells infected with TIGR4 or EF3030 and subsequently treated with CCCP exhibited complete ΔΨm dissipation (Figs. 6F, 6G, 6I), confirming that lung epithelial cells maintain an intact ΔΨm despite Spn infection over this

timeframe. No significant changes in ΔΨm were observed in cells infected with TIGR4ΔspxBΔlctO or EF3030ΔspxBΔlctO compared to their wild-type counterparts, indicating that Spn-derived H_2O_2 does not substantially affect ΔΨm under these conditions.

To evaluate cytotoxicity, the same population of infected A549 cells was analyzed using SYTOX Blue staining and flow cytometry. Compared to mock-infected controls, no significant reduction in cell viability was observed in A549 cells infected with TIGR4 or its H_2O_2-deficient mutant TIGR4ΔspxBΔlctO (Fig. 6H). In contrast, infection with EF3030 resulted in a significant decrease in cell viability relative to mock-infected controls and the corresponding H_2O_2-deficient mutant EF3030Δ*spxB*Δ*lctO* (Fig. 6F). Collectively, these results suggest that Spn infection does not substantially impair ΔΨm, consistent with H_2O_2 targeting TCA cycle enzymes (e.g., ACO2, GDH, OGDHC; Figs. 3C–F, 4D–F) rather than ETC complexes, thereby preserving mitochondrial membrane integrity over the observed timeframe.

Spn-Derived H_2O_2 modulates limited alveolar apoptosis via TCA cycle Inhibition.

Having established that Spn-derived H_2O_2 inhibits the TCA cycle without compromising mitochondrial membrane potential (ΔΨm) in lung epithelial cells, we next investigated whether this metabolic disruption induces cell death by impairing OXPHOS. Apoptosis was assessed using the terminal deoxynucleotidyl transferase biotin-dUTP nick end labeling (TUNEL) assay, which detects DNA fragmentation—a hallmark of late-stage apoptosis—through fluorescent labeling of 3'-OH termini in fragmented DNA, enabling quantitative assessment of apoptotic cell populations via confocal microscopy. Mock-infected A549 alveolar epithelial cells exhibited negligible DNA fragmentation, whereas DNase I-treated cells, a positive control, displayed a

397 significant increase in fluorescence intensity, predominantly in nuclear regions (Fig. 7A and
398 7B), confirming assay.

399 A549 cells were infected for 10 hours with wild-type Spn strains TIGR4 and EF3030, or
400 their H_2O_2-deficient mutants TIGR4ΔspxBΔlctO and EF3030ΔspxBΔlctO. While TUNEL-
401 positive cells were infrequent across all infected conditions (Fig. 7A), the apoptotic signal in
402 infected cells was significantly higher than in mock-infected controls (Fig. 7B, 7C), yet
403 markedly lower than in DNase I-treated cells. Notably, cells infected with H_2O_2-producing
404 strains TIGR4 and EF3030 exhibited a significantly greater apoptotic signal compared to those
405 infected with H_2O_2-deficient mutants (Fig. 7C), indicating that Spn-derived H_2O_2 enhances cell
406 death. These findings suggest that H_2O_2-mediated inhibition of TCA cycle enzymes (e.g.,
407 ACO2, GDH, OGDHC), which supply electron donors for OXPHOS, contributes to limited
408 apoptosis, consistent with the minimal $\Delta\Psi m$ disruption observed previously. The strain-specific
409 cytotoxicity observed with EF3030 (Fig. 6F) likely involves additional virulence factors beyond
410 H_2O_2 production, given its greater impact on cell viability compared to TIGR4.

411 To further explore the role of H_2O_2 in apoptosis, A549 cells were treated with 2 mM
412 H_2O_2 every 2 hours for 8 hours, simulating the delayed accumulation of Spn-derived H_2O_2
413 during infection, which becomes detectable after 4 hours as cellular substrates are depleted[5].
414 TUNEL analysis revealed that the apoptotic signal in H_2O_2-treated cells was comparable to
415 that in wild-type Spn-infected cells but significantly lower than in DNase I-treated controls (Fig.
416 7A, 7C). These results confirm that Spn-derived H_2O_2 contributes to limited alveolar cell
417 apoptosis, likely via metabolic stress from TCA cycle inhibition, though its effect is less
418 pronounced than that of canonical apoptosis inducers.

Gene expression analysis revealed a complex interplay of apoptosis regulation in human bronchial cells infected with H_2O_2-producing strains TIGR4 and TIGR4Δ*lctO* compared to mock-infected controls and the H_2O_2-deficient mutant TIGR4Δ*spxB* (Fig. 7D and Supplemental Table 2). Pro-apoptotic genes, including FAS and BBC3, were significantly upregulated in TIGR4-infected cells ($\log_2$ fold-change [FC] 1–6; FDR < 0.05), promoting apoptosis via death receptor signaling and stress response pathways. Concurrently, anti-apoptotic genes such as BCL2A1 (BCL2-family member, prevent Cytc release) and TRAF1 were also upregulated, likely counteracting cell death by inhibiting caspase activation and enhancing survival through NF-kappaB signaling (NFKB1). This dual upregulation of pro- and anti-apoptotic genes, absent in TIGR4Δ*spxB*-infected cells, likely underlies the limited apoptosis observed in the TUNEL assay, as the balance between these opposing pathways mitigates extensive cell death despite *spxB*-mediated H_2O_2 stress (Fig. 6A–C). Furthermore, gene ontology analysis of cell death-related genes revealed that TIGR4 and TIGR4Δ*lctO* dysregulated 412 and 307 genes (Supplemental Table 2), respectively, whereas only 26 genes were dysregulated in TIGR4Δ*spxB*-infected cells, underscoring the pivotal role of *spxB* in driving apoptosis-related transcriptional reprogramming. This pro- and anti-apoptotic balance mirrors patterns in MYC-induced cancer biology[50].

Discussion

This study unveils a novel and unique mechanism by which Spn disrupts host cell metabolism through H_2O_2-mediated inhibition of the TCA cycle, coupled with extensive transcriptional and metabolic reprogramming in lung epithelial cells. To our knowledge, direct inhibition of the TCA cycle by a bacterial pathogen has not been described prior to this work,

positioning Spn's H_2O_2-driven metabolic disruption as a groundbreaking insight into pneumococcal pathogenesis. Spn-derived H_2O_2, primarily produced by pyruvate oxidase (SpxB), targets key TCA cycle enzymes—aconitase (ACO2), glutamate dehydrogenase (GDH), and α-ketoglutarate dehydrogenase (OGDHC)—significantly inhibiting their activities. This leads to citrate accumulation, as evidenced by elevated intracellular and extracellular citrate levels in TIGR4-infected Calu-3 cells compared to mock-infected controls or cells infected with the H_2O_2-deficient mutant TIGR4ΔspxBΔlctO.

This metabolic bottleneck downstream of citrate synthase impairs NADH and $FADH_2$ production, critical electron donors for oxidative phosphorylation (OXPHOS), aligning with the observed inhibition of CIDR at H_2O_2-concentrations as low as 5 μM. In contrast, CIIDR, which utilizes substrates acting downstream of the enzymes inhibited by Spn-H_2O_2, required higher concentrations (25 μM) for inhibition. Notably, the absence of significant changes in electron transport chain (ETC) complex activities (Fig. 3G) underscores that Spn-H_2O_2 targets upstream TCA cycle enzymes rather than the ETC itself, a mechanism distinct from the ETC decline associated with human diseases like neurodegeneration, cancer, and diabetes[51].

The hallmark of pneumococcal disease is Spn's ability to invade host cells and manipulate their metabolism to establish infection[52]. Our findings demonstrate that H_2O_2-mediated inhibition of the TCA cycle disrupts host energy metabolism and induces transcriptional reprogramming, shifting lung epithelial cells toward a Warburg-like phenotype[53] that fosters bacterial proliferation. The NAD^+ salvage pathway, which supplies electron donors for host antibacterial responses against Spn[48], is likely impaired by reduced NADH production resulting from TCA cycle suppression. This metabolic disruption compromises host defenses, enabling Spn to exploit host resources, as evidenced by significant glucose depletion in

TIGR4-infected Calu-3 cells. Furthermore, transcriptional reprogramming in TIGR4-infected cells, with 2,684 genes dysregulated compared to 163 in TIGR4ΔspxB-infected cells, amplifies this metabolic shift. Upregulation of glycolysis-associated genes (HK2, PFKP, HIF1A) and downregulation of pyruvate dehydrogenase complex regulators (PC, PDK2, PDPR) indicate a Warburg-like metabolic switch toward glycolysis[53], likely a compensatory response to H_2O_2-induced mitochondrial dysfunction. This reprogramming, absent in TIGR4ΔspxBΔlctO-infected cells, underscores the critical role of SpxB in driving host metabolic stress.

Spn- H_2O_2 induces mitochondrial aggregation and apical migration in A549 cells (Fig. 2B–C) and Calu-3 cells (not shown), indicative of disrupted mitochondrial dynamics that amplify oxidative stress. The interaction between the cytoskeleton and the mitochondrial outer membrane is critical for regulating mitochondrial respiration[54]. Mutations in microtubule-associated proteins, such as plectin or desmin, impair mitochondrial network integrity, and similarly, Spn-H_2O_2-mediated microtubule disruption, absent in H_2O_2-deficient mutants[17,23], likely drives mitochondrial aggregation and mislocalization in lung epithelial cells, potentially contributing to metabolic dysfunction. Supporting this, the absence of βII-tubulin in cardiomyocytes correlates with a shift to glycolysis-dependent metabolism (Warbug effect)[55]. The increased extracellular lactate and acetate in TIGR4-infected cells (Fig. 5E–F) reflect Spn's manipulation of host glycolytic flux, potentially fueling bacterial metabolism while stressing host cells. Notably, mitochondrial membrane potential ($\Delta\Psi m$) remains intact in TIGR4- and EF3030-infected cells, indicating that H_2O_2 targets TCA cycle enzymes rather than ETC complexes or membrane integrity. This preservation of $\Delta\Psi m$ aligns with the limited apoptosis observed in TUNEL assays, where TIGR4- and EF3030-infected cells showed significantly higher apoptotic signals than H_2O_2-deficient mutants but far less than DNase I-

treated controls. The balanced upregulation of pro-apoptotic (FAS, BBC3) and anti-apoptotic (BCL2A1, TRAF1) genes in TIGR4-infected cells likely mitigates extensive cell death, enabling Spn to maintain host cell viability for sustained infection.

The decline in ETC activity is a hallmark of many human diseases, yet our study uniquely demonstrates that Spn directly targets the TCA cycle, upstream of the ETC, to disrupt host metabolism. The oxidation of cytochrome c (Cytc) by Spn-H_2O_2, forming tyrosyl radicals, further impairs mitochondrial function by disrupting electron transfer, amplifying ROS production, and exacerbating metabolic stress. This mechanism not only enhances Spn's virulence but also parallels metabolic disruptions, suggesting broader implications for understanding host-pathogen interactions.

In conclusion, Spn employs H_2O_2-mediated inhibition of the TCA cycle as a novel strategy to reprogram host cell metabolism and the transcriptional profiles, thereby facilitating bacterial invasion and persistence. By disrupting NADH production and inducing glycolytic reprogramming, Spn impairs host antibacterial responses, including those dependent on the NAD^+ salvage pathway[48], while enhancing its own survival. These findings underscore the therapeutic potential of targeting SpxB activity, such as through SpxB inhibitors, or restoring TCA cycle function to attenuate pneumococcal disease severity. Recent evidence suggests that enhancing host cell NAD^+ metabolism can suppress Spn replication[48]. Future studies should delineate the molecular interactions between H_2O_2 and TCA cycle enzymes, investigate the role of host antioxidant defenses in mitigating Spn-induced metabolic stress, and employ in vivo models to elucidate how Spn's metabolic manipulation drives disease progression. Such investigations may inform the development of innovative therapeutic strategies for pneumococcal infections.

Material and Methods

Bacterial strains, growth conditions, and preparation of inoculum. Spn strains utilized in this study are listed in Table 1. Strains were cultured on blood agar plates (BAP) containing 5% sheep's blood from frozen bacterial stocks stored in skim milk, tryptone, glucose, and glycerin (STGG)[56] or in Todd-Hewitt broth supplemented with 0.5% (w/v) yeast extract (THY) and incubated at 37°C with 5% CO_2. Inoculum for experiments was prepared as previously described[9]. Overnight cultures of Spn on BAP were harvested in phosphate buffered saline (PBS) (pH 7.4), the OD_{600} of this suspension was obtained and adjusted to a final 0.1 density that contained ~5.15 x 10^8 cfu/ml.

Cell cultures. A549 human type II alveolar epithelial cells (ATCC, CCL-185) were cultured in Dulbecco's Modified Eagle's Medium (DMEM) (Gibco) supplemented with 10% fetal bovine serum (FBS), 2 mM L-glutamine (Gibco), and 100 U/mL of penicillin-streptomycin (Gibco) in 25 cm^2 flasks (Fisher). Calu-3 cells (ATCC, HTB-55) were cultured in Eagle's Minimum Essential Medium [EMEM, (American Type Culture Collection, ATCC)] supplemented with 10% FBS and 100 U/mL of penicillin-streptomycin (Gibco). Cell passages were performed by trypsinization with Trypsin-EDTA (0.25%), phenol red (Gibco). Cells were incubated at 37°C with 5% CO_2 and were supplemented with fresh medium 2-3 times weekly and passaged to a new flask weekly or when cells reached ~100% confluency.

Infection of human bronchial and alveolar cells with *S. pneumoniae* strains. Cell infection experiments were performed using cells cultured for 8-10 days in the specified device. Cells were grown in 6-well plates with glass cover slips (Genesee, Fisher) or 8-well glass slides (Thermo Fisher Scientific, Nunc Lab-Tek II CC2) at 37°C with 5% CO_2. Prior to infection, cells

were washed three times with sterile PBS and then incubated in infection media consisting of DMEM or EMEM, supplemented with 5% FBS, 2 mM L-glutamine, and 1X HEPES (Gibco). Cells were infected with Spn strains, mutant derivatives, or along with appropriate controls, and incubated at 37°C with 5% CO_2 for various time points.

Cytochrome c Oxidation Assay. To analyze the oxidation and degradation of heme in cytochrome c (Cytc) by Spn-H_2O_2, THY supplemented with 56 µM Cytc from horse heart (Sigma) was inoculated with Spn and incubated for 6 hours at 37°C with 5% CO2 in a 6-well plate. Supernatants were collected, centrifuged at 4°C for 5 minutes at 25,200×g, and transferred to a 96-well plate. The plate was then analyzed by spectroscopy, spanning wavelengths from 200 nm to 1000 nm, using an SYN H1 Hybrid Biotek reader (Agilent). As a control, 500 units (U) of catalase were added to a well containing THY-Cytc and Spn.

Detection of radicals by spin-trapping. DEPMPO [5-(Diethoxyphosphoryl)-5-methyl-1-pyrroline-N-oxide, 98%, Cayman Chemical, P/N 10006435] was utilized to detect and identify the formation of radical species. Spn was cultured in THY and incubated for 4 h at 37°C. As a control, uninfected THY was incubated in the same condition. After incubation, the cell suspension was micro-centrifuged, and 32 µL of supernatant was used for each spin-trapping sample. The final reaction mixture contained, when added, 30 mM DEPMPO and 56 µM Cyt*c*, in a volume of 40 µL. Spn-H_2O_2 free sample was obtained by pretreating the bacterial supernatant liquid with 100 U catalase for 1 minute. Methods of radical detection are performed as mentioned previously[5].

Fluorescent staining of alveolar cells. A549 cells seeded in a 6-well plate with glass coverslips were washed and added with infection media as mentioned above. Cells were then infected with Spn and incubated for 4, 6, or 8 h. After incubation with Spn, cells were fixed with

2% paraformaldehyde, permeabilized with 0.5% Triton X100, and blocked with 2% bovine serum albumin (BSA) following a previously described protocol[5]. Post-blocking, cellular mitochondria were stained with an anti-mitochondria monoclonal antibody (Invitrogen) at a concentration of 2 µg/mL in 2% BSA for 1 h. Cells were then washed with PBS and incubated for 1 h with a secondary goat anti-mouse FITC (SouthernBiotech) at a concentration of 20 µg/mL and phalloidin (7 units) in 2% BSA for 1 h. Cells were then washed, coverslips removed from wells, let dry, mounted and stained for DNA using ProLong Diamond antifade mountant containing DAPI (50 µg/mL). Slides were then imaged using a confocal microscope Nikon A1R HD25 laser scanning confocal upright microscope. Confocal images were analyzed using Imaris x64 software version 10.1.0.

Bulk RNA sequencing analysis. Human bronchial Calu-3 cells were seeded in 100 mm tissue culture treated dishes (Fisher) and incubate until they became polarized, 10-day post seeding. Cells were washed three times with sterile PBS and infected with Spn, mutant derivatives, or mock-infected, and incubated for 4 h at 37°C in a 5% CO_2 atmosphere. After incubation, supernatant containing planktonic pneumococci were removed, the infected cells were harvested in one ml TRIzol (Invitrogen) and immediately flash frozen at -80°C. The following procedures were performed by the UMMC Molecular and Genomics Core Facility (www.umc.edu/genomicscore). RNA was extracted using the Pure Link RNA Mini Kit from archived samples (Invitrogen) according to manufacturer instructions and assessed for quality control parameters of minimum concentration and fidelity (i.e. 18S and 28S bands, RIS >8) through the UMMC Molecular and Genomics Core Facility (MGCF). Libraries were prepared for RNA sequencing per detailed protocols from Illumina mRNA stranded kit. Briefly, a pooled library was prepared from using n=12-24 samples per group using TruSeq mRNA Stranded

Library Prep Kit (Set-A-indexes), quantified with the Qubit Fluorometer (Invitrogen), and assessed for quality and size Qiagen QIAxcel Advanced System or Agilent TapeStation. The library was sequenced using the NextSeq 2000 using P3 (200 cycles, paired end 100bp) on the Illumina NextSeq 2000 platform. Sequenced reads were assessed for quality using the Illumina BaseSpace Cloud Computing Platform and/or custom analysis pipeline and FASTQ sequence files were aligned reads to the reference genome (e.g., Ensembl/Hg38, Rnor_6.0, etc.) using DRAGEN RNA Pipeline Application (v.3.7.5) or custom analysis pipelines developed through MGCF. Differential expression was determined using DRAGEN Differential Expression Application (v.3.10.4) of DESeq2. Gene Set Enrichment Analysis was performed using Reactome analysis tools (https://reactome.org/) or other databases. Data was deposited into NCBI GEO data under accession number ####.

Gene expression study deposited in NCBI-GEO (GSE195778)[48] was utilized to investigate the expression of genes in the D39 background. We focused on RNA data from human bronchial epithelial cell line Beas-2B were infected with Spn at multiplicity of infection (MOI) of 1 for 9 or 16 h, and compared against the mock-infected control.

To elucidate the biological implications of Spn infection, functional enrichment analysis was performed on differentially expressed genes (DEGs) using DAVID (v2023q1) and g:Profiler (v.e109_eg56_p17). DAVID and g:Profiler were used to identify enriched Gene Ontology (GO) terms across three categories: Biological Process (BP), Molecular Function (MF), and Cellular Component (CC). In TIGR4-infected Calu-3 cells, GO-BP analysis revealed significant enrichment of terms related to "mitochondrial organization" (GO:0007005, FDR = 2.3e-04), "cellular response to oxidative stress" (GO:0034599, FDR = 8.7e-03), and "apoptotic process" (GO:0006915, FDR = 1.2e-02), consistent with Spn-H_2O_2-induced mitochondrial

dysfunction and limited apoptosis. GO-CC terms highlighted "mitochondrial inner membrane" (GO:0005743, FDR = 4.5e-03) and "respiratory chain complex" (GO:0098803, FDR = 9.1e-03), aligning with the observed inhibition of CIDR. KEGG pathway analysis via DAVID identified downregulation of the TCA cycle pathway (hsa00020, FDR = 3.8e-03) in TIGR4-infected cells, corroborating the inhibition of TCA cycle enzymes like ACO2 and OGDHC, while the "Glycolysis/Gluconeogenesis" pathway (hsa00010, FDR = 1.1e-02) was upregulated, reflecting the enhanced glycolysis observed (e.g., HK2 upregulation). Complementary analysis using g:Profiler provided additional insights into molecular networks. The "oxidative phosphorylation" pathway (KEGG:00190, p-adj = 2.4e-03) was significantly downregulated in TIGR4-infected cells, consistent with CIDR inhibition, while "response to reactive oxygen species" (GO:0000302, p-adj = 5.6e-03) was enriched, supporting the upregulation of oxidative stress response genes (SOD2, TXNRD2). Notably, in TIGR4Δ*spxB*Δ*lctO*-infected cells, these pathways showed minimal perturbation, underscoring the role of H_2O_2 in driving these changes.

Heart mitochondria isolation. Intact rat heart mitochondria were isolated from Sprague Dawley rats similar to published methods [57,58]. In brief, heart tissue was minced with a razor blade in 500 µL of MSM buffer (220 mM mannitol, 70 mM sucrose, 5 mM MOPS pH 7.4) supplemented with 2 mg/mL bacterial proteinase type XXIV. The minced tissue was added to 5 mL of ice-cold isolation buffer (MSM buffer supplemented with 2 mM EDTA and 0.2% fatty acid-free BSA) and homogenized on ice with a glass homogenizer and a Teflon pestle for 4 strokes. To inhibit the proteinase, 0.1 mM phenylmethylsulfonyl fluoride (PMSF) was used. The tissue homogenate was centrifuged at 300×g for 10 min at 4°C. The supernatant was then

centrifuged at 3000×g for 10 min at 4 °C, and the mitochondrial pellet washed once in ice-cold MSM buffer. Protein concentration was determined by using the BioRad DC protein assay.

Hydrogen peroxide quantification. H_2O_2 levels were quantified from culture supernatants of different Spn strains. Each strain and culture condition were assessed in duplicate in 6-well plates and incubated for 4 hours at 37°C with 5% CO_2. Cultures were then collected, centrifuged for 5 minutes at 25,200×g, and the supernatants were filter-sterilized using syringe filters (0.2 µm pore size). H_2O_2 was quantified using the Amplex Red H_2O_2 assay kit (Molecular Probes), according to the manufacturer's instructions. Measurements were taken using an SYN H1 Hybrid Biotek reader (Agilent) or an Oroboros O2k FluoRespirometer[59].

Animal information. Sprague Dawley rats were purchased from Jackson Laboratory (Maine, US) at 7 weeks of age and allowed to acclimate for at least 1 week before use. All animals were housed in the Center for Comparative Research animal facilities of the University of Mississippi Medical Center (UMMC). Animals were kept on a 12 h light/12 h dark cycle and fed a standard laboratory rodent diet (Teklad 8640). All procedures were conducted in accordance with the National Institutes of Health's Guide for the Care and Use of Laboratory Animals and approved by the UMMC Institutional Animal Care and Use Committee (Protocol #1582).

Experiments of mitochondrial respiration and mitochondrial complex activity. Measurement of mitochondrial respiration follows previously published protocols[57,58]. In brief, Spn strains were cultured in THY for 4 h 37°C with a 5% CO_2 atmosphere. Sterilized supernatants from each sample were then used to measure mitochondrial respiration driven through complex-I and II and activity through complexes I, II, III, and IV. Complex-I driven respiration was measured through 20 mM glutamate plus 5 mM malate or 10 mM pyruvate plus 5 mM malate substrates with addition of 2 mM ADP. Complex-II driven respiration was

648 measured through 20 mM succinate as the substrates with addition of 2 mM ADP. All
649 measurements were performed in an Oroboros O2K FluoRespirometer. All samples were
650 normalized to protein content as determined by BioRad DC assay and reported as nmol e-
651 /min/mg prot. *Complex I* activity was measured as the time-dependent oxidation of NADH at
652 340 nm using a measured extinction coefficient of 6.22 $mM^{-1}cm^{-1}$. The reaction mixture in a
653 regular quartz cuvette contained 10 mM KPi, 5 mM $MgCl_2$, 30 mM KCl, 1 mM EDTA, 75 mM
654 Tris, pH 7.5, 100 µM Coenzyme Q1 (CoQ1), 5 µM antimycin A, and 5 µL heart mitochondria in
655 a final volume of 2 mL. The reaction was initiated by adding 100 µM NADH and the fastest
656 rates were obtained after NADH was added. *Complex II* activity was measured as the time-
657 dependent oxidation of 2,6-dichloroindophenol sodium salt hydrate (DCPIP) at 600 nm using a
658 measured extinction coefficient of 19.1 $mM^{-1}cm^{-1}$. The reaction mixture in a micro-cuvette
659 contained 10 mM Kpi, 5 mM $MgCl_2$, 30 mM KCl, 1 mM EDTA, 75 mM Tris, pH 7.5, 20 mM
660 succinate, 80 µM DCPIP, 1 mM KCN, 5 µM Antimycin A, 4 µM rotenone, and 5 µL of heart
661 mitochondria in a final volume of 200 µL. Reactions were initiated by adding 50 µM
662 decylubiquinone and the linear rates were obtained. *Complex III* activity was measured as the
663 time-dependent reduction of cytochrome *c* at 550 nm using a measured extinction coefficient
664 of 18.7 $mM^{-1}cm^{-1}$. The reaction mixture in a regular glass cuvette contained 10 mM Kpi, 5 mM
665 $MgCl_2$, 30 mM KCl, 1 mM EDTA, 75 mM Tris, pH 7.5, 3 mM KCN, 4 µM rotenone, 60 µM
666 cytochrome *c*, 5 µL of heart mitochondria in a final volume of 2 mL. *Complex IV* activity was
667 measured as the time-dependent oxidation of N,N,N',N'-Tetramethyl-p-phenylenediamine
668 dihydrochloride (TMPD) to donate electrons to cytochrome *c*. The reaction mixture in a cuvette
669 contained 50 mM Tris, 8 mM KCl, 1 mM EDTA, 16 µg/µL catalase, pH 7.4, 3 mM ascorbate,
670 0.3 mM TMPD, and 25 µM cytochrome c. Reactions were initiated with 100 µM reduced

decylubiquinone. The rate was linear for 1-2 min. *Aconitase* activity was measured as the time-dependent formation of cis-aconitate at 240 nm using a measured extinction coefficient of 2.2 $mM^{-1}cm^{-1}$ [60]. The reaction mixture in a quartz cuvette containing 50 mM Tris–HCl (pH 7.4) containing 0.6 mM MnCl2, 30 mM citrate, and 0.2% peroxide-free Triton-X 100. For each enzyme, the inhibited non-enzymatic background rates were subtracted from the enzymatic rates. *Glutamate dehydrogenase* and *α-ketoglutarate dehydrogenase* were measured using the kits from Sigma (MAK099 and MAK189) following the provided protocols.

JC-1 assay. To measure mitochondrial membrane potential in human alveolar A549 cells infected with Spn, the MitoProbe JC-1 assay kit (Invitrogen) was used. A549 cells grown in a 6-well plate were washed and treated with infection media as described above. Cells were then infected with Spn and incubated for 10 hours. After incubation, cells were lifted from the wells using 0.25% Trypsin-EDTA, counted, and ~1×10^6 cells were used for JC-1 staining following the manufacturer's protocol. As a control, uninfected cells were treated with 125 μM Carbonyl cyanide m-chlorophenyl hydrazone (CCCP) for 10 minutes or 2 mM H_2O_2 for 1 hour. After JC-1 staining, cells were also stained for dead cells with 1 μM SYTOX Blue dead cell stain (Invitrogen). Cell samples were then analyzed using a NovoCyte flow cytometer with a threshold of 50,000 events. JC-1 analysis utilized PE-Texas Red with 596 nm emission and FITC with 498 nm emission, while SYTOX Blue dead cell stain was detected with AmCyan at 498 nm emission. Cells were analyzed using NovoExpress software, with a 20% compensation applied to the FITC channel.

TUNEL assay. T To identify late-stage apoptosis in Spn-infected human alveolar A549 cells, the Click-iT Plus TUNEL assay kit (Invitrogen) was utilized. A549 cells were seeded in a 6-well plate with glass coverslips and used after ~7-10 days post-seeding. Before infection, A549

cells were washed and treated with infection media as described above. Cells were then infected with the indicated Spn strain and incubated for 8 hours. As a control, some cells were treated with 2 mM H_2O_2 every 2 hours for 8 hours. After incubation, cells were stained following the manufacturer's protocol. Following staining, cells were washed, coverslips were removed, and the cells were allowed to dry before being mounted and stained for DNA using ProLong Gold Antifade Mountant containing DAPI. Slides were then imaged using a Nikon A1R HD25 laser scanning confocal upright microscope. Confocal images were analyzed using Imaris x64 software version 10.1.0.

Activity of glutamate dehydrogenase in bronchial Calu-3 cells infected with pneumococcal strains. Calu-3 cells grown in 100 mm tissue culture-treated dishes (Fisher) were washed three times with sterile PBS to remove antibiotics and then added with 10 ml of infection medium, consisting of EMEM supplemented with 1% HEPES buffer and 5% fetal bovine serum (FBS). Cells were either mock-infected or infected with TIGR4 or TIGR4ΔspxBΔlctO and incubated for 8 hours at 37°C in a 5% CO_2 atmosphere. The supernatant, containing the planktonic bacterial fraction, was collected for HPLC studies, as detailed below. Infected cells were washed once with PBS and harvested using a cell scraper in 1 ml of cold sterile PBS. The cells were centrifuged at 300 × g for 5 minutes, and the resulting pellet was resuspended in 200 µl of PBS. The cells were then lysed using a Dounce homogenizer, and the lysate volume was adjusted to 600 µL with sterile PBS. The lysate was centrifuged at 10,000 × g for 15 minutes at 4°C, and the soluble fraction was used to assess the enzymatic activity of glutamate dehydrogenase (GDH) and for HPLC analysis. Assays were performed in technical triplicates with two biological replicates.

Glutamate dehydrogenase activity and metabolite quantification in Spn-infected human respiratory cells. Human bronchial Calu-3 cells were cultured for 10 days in 55 cm² Petri dishes in Eagle's Minimum Essential Medium (EMEM) supplemented with 1% HEPES buffer and 5% fetal bovine serum (FBS). Cells were washed three times with sterile phosphate-buffered saline (PBS) to remove antibiotics and overlaid with 10 ml of infection medium (EMEM with 1% HEPES and 5% FBS). Cells were infected with Spn strains and incubated at 37°C for 8 h. Mock-infected cells served as controls. For secreted metabolite analysis, 1 ml of infection medium was centrifuged at 10,000 × g for 5 min to remove planktonic bacteria, and the supernatant was collected. Cells were washed once with PBS, scraped in 1 ml PBS, and centrifuged at 300 × g for 5 min. For glutamate dehydrogenase (GDH) activity, the cell pellet was resuspended in 200 µl PBS, homogenized using a Dounce homogenizer, diluted with 400 µl PBS, and centrifuged at 10,000 × g for 15 min. The resulting supernatant (cell extract) was used for GDH activity assays and intracellular metabolite quantification. GDH activity was measured using a non-radioactive colorimetric assay (MAK499-1KT, Sigma-Aldrich, St. Louis, MO) according to the manufacturer's instructions. For metabolite quantification, lactate, acetate, and citrate levels in cell-free supernatants (extracellular) and cell extracts (intracellular) were analyzed by high-performance liquid chromatography (HPLC) using a Thermo Dionex Ultimate 3000 UHPLC System equipped with an Aminex HPX-87H column (Bio-Rad, Hercules, CA) maintained at 25°C. An isocratic elution was performed with 5 mM H_2SO_4 at a flow rate of 0.6 mL/min, and metabolites were detected at 208 nm. Samples were prepared by mixing 100 µl of supernatant or cell extract with 100 µl of 95% ethanol, incubating at –80°C for 15 min to precipitate proteins, and centrifuging at 20,000 × g for 15 min. A 20 µl aliquot of the resulting supernatant was injected for analysis. All assays were performed with

technical triplicates and two biological replicates. Statistical analyses are described in the relevant figure legends.

Statistical analysis. We performed one-way analysis of variance (ANOVA) followed by Dunnett's multiple-comparison test when two or more groups were involved. All analysis was performed using GraphPad Prism software (version 10.2.1).

ACKNOWLEDGEMENTS

This study was supported in part by grants from the National Institutes of Health (NIH), including R21AI144571, 1R01AI175461-01A1 (to J.E.V.) and R01GM142113 and RR17767 (to K.W.). Confocal microscopy and mitochondrial respiration studies (K.E.) were supported by the National Institute of General Medical Sciences (NIGMS) under Award Number P20GM121334. J.E.V. is also supported by NIGMS through the Molecular Center of Health and Disease (P20GM144041). RNA-seq data analysis was performed at the UMMC Molecular and Genomics Facility, supported by funds from NIGMS (P20GM144041), Mississippi INBRE (P20GM103476), the Obesity, Cardiorenal, and Metabolic Diseases COBRE (P30GM149404), and the Mississippi Center of Perinatal Research (P20GM121334). The content is solely the responsibility of the authors and does not necessarily represent the official views of the NIH or the U.S. Department of State. The authors thank Dr. David Brown (UMMC) for his assistance with confocal microscopy.

DISCLOSURE STATEMENTS

The authors report that there are no competing interests to declare.

References

1. Kadioglu, A., Weiser, J.N., Paton, J.C., and Andrew, P.W. (2008). The role of Streptococcus pneumoniae virulence factors in host respiratory colonization and disease. Nat Rev Microbiol *6*, 288-301. 10.1038/nrmicro1871.
2. van der Poll, T., and Opal, S.M. (2009). Pathogenesis, treatment, and prevention of pneumococcal pneumonia. Lancet *374*, 1543-1556. 10.1016/S0140-6736(09)61114-4.
3. Feldman, C., Anderson, R., Cockeran, R., Mitchell, T., Cole, P., and Wilson, R. (2002). The effects of pneumolysin and hydrogen peroxide, alone and in combination, on human ciliated epithelium in vitro. Respir Med *96*, 580-585. 10.1053/rmed.2002.1316.
4. Rai, P., Parrish, M., Tay, I.J., Li, N., Ackerman, S., He, F., Kwang, J., Chow, V.T., and Engelward, B.P. (2015). Streptococcus pneumoniae secretes hydrogen peroxide leading to DNA damage and apoptosis in lung cells. Proc Natl Acad Sci U S A *112*, E3421-3430. 10.1073/pnas.1424144112.
5. Scasny, A., Alibayov, B., Khan, F., Rao, S.J., Murin, L., Jop Vidal, A.G., Smith, P., Li, W., Edwards, K., Warncke, K., and Vidal, J.E. (2023). Oxidation of hemoproteins by Streptococcus pneumoniae collapses the cell cytoskeleton and disrupts mitochondrial respiration leading to the cytotoxicity of human lung cells. Microbiol Spectr, e0291223. 10.1128/spectrum.02912-23.
6. Bogaert, D., De Groot, R., and Hermans, P.W. (2004). Streptococcus pneumoniae colonisation: the key to pneumococcal disease. Lancet Infect Dis *4*, 144-154. 10.1016/S1473-3099(04)00938-7.
7. Lisher, J.P., Tsui, H.T., Ramos-Montanez, S., Hentchel, K.L., Martin, J.E., Trinidad, J.C., Winkler, M.E., and Giedroc, D.P. (2017). Biological and Chemical Adaptation to

Endogenous Hydrogen Peroxide Production in Streptococcus pneumoniae D39. mSphere *2*. 10.1128/mSphere.00291-16.

8. Pericone, C.D., Park, S., Imlay, J.A., and Weiser, J.N. (2003). Factors contributing to hydrogen peroxide resistance in Streptococcus pneumoniae include pyruvate oxidase (SpxB) and avoidance of the toxic effects of the fenton reaction. J Bacteriol *185*, 6815-6825. 10.1128/JB.185.23.6815-6825.2003.

9. Wu, X., Gordon, O., Jiang, W., Antezana, B.S., Angulo-Zamudio, U.A., Del Rio, C., Moller, A., Brissac, T., Tierney, A.R.P., Warncke, K., et al. (2019). Interaction between Streptococcus pneumoniae and Staphylococcus aureus Generates (.)OH Radicals That Rapidly Kill Staphylococcus aureus Strains. J Bacteriol *201*. 10.1128/JB.00474-19.

10. Mraheil, M.A., Toque, H.A., La Pietra, L., Hamacher, J., Phanthok, T., Verin, A., Gonzales, J., Su, Y., Fulton, D., Eaton, D.C., et al. (2021). Dual Role of Hydrogen Peroxide as an Oxidant in Pneumococcal Pneumonia. Antioxid Redox Signal *34*, 962-978. 10.1089/ars.2019.7964.

11. Shenoy, A.T., Brissac, T., Gilley, R.P., Kumar, N., Wang, Y., Gonzalez-Juarbe, N., Hinkle, W.S., Daugherty, S.C., Shetty, A.C., Ott, S., et al. (2017). Streptococcus pneumoniae in the heart subvert the host response through biofilm-mediated resident macrophage killing. PLoS pathogens *13*, e1006582. 10.1371/journal.ppat.1006582.

12. Brissac, T., Shenoy, A.T., Patterson, L.A., and Orihuela, C.J. (2017). Cell invasion and pyruvate oxidase derived H2O2 are critical for Streptococcus pneumoniae mediated cardiomyocyte killing. Infection and immunity. 10.1128/IAI.00569-17.

13. Ramos-Montanez, S., Tsui, H.C., Wayne, K.J., Morris, J.L., Peters, L.E., Zhang, F., Kazmierczak, K.M., Sham, L.T., and Winkler, M.E. (2008). Polymorphism and regulation

of the spxB (pyruvate oxidase) virulence factor gene by a CBS-HotDog domain protein (SpxR) in serotype 2 Streptococcus pneumoniae. Mol Microbiol *67*, 729-746. 10.1111/j.1365-2958.2007.06082.x.

14. Echlin, H., Frank, M.W., Iverson, A., Chang, T.C., Johnson, M.D., Rock, C.O., and Rosch, J.W. (2016). Pyruvate Oxidase as a Critical Link between Metabolism and Capsule Biosynthesis in Streptococcus pneumoniae. PLoS pathogens *12*, e1005951. 10.1371/journal.ppat.1005951.

15. Spellerberg, B., Cundell, D.R., Sandros, J., Pearce, B.J., Idanpaan-Heikkila, I., Rosenow, C., and Masure, H.R. (1996). Pyruvate oxidase, as a determinant of virulence in Streptococcus pneumoniae. Mol Microbiol *19*, 803-813. 10.1046/j.1365-2958.1996.425954.x.

16. Rubins, J.B., Duane, P.G., Clawson, D., Charboneau, D., Young, J., and Niewoehner, D.E. (1993). Toxicity of pneumolysin to pulmonary alveolar epithelial cells. Infect Immun *61*, 1352-1358. 10.1128/iai.61.4.1352-1358.1993.

17. Scasny, A., Alibayov, B., Khan, F., Rao, S.J., Murin, L., Jop Vidal, A.G., Smith, P., Wei, L., Edwards, K., Warncke, K., and Vidal, J.E. (2023). Oxidation of hemoproteins by Streptococcus pneumoniae collapses the cell cytoskeleton and disrupts mitochondrial respiration leading to cytotoxicity of human lung cells. bioRxiv. 10.1101/2023.06.07.544089.

18. Gao, Y., Xu, W., Dou, X., Wang, H., Zhang, X., Yang, S., Liao, H., Hu, X., and Wang, H. (2019). Mitochondrial DNA Leakage Caused by Streptococcus pneumoniae Hydrogen Peroxide Promotes Type I IFN Expression in Lung Cells. Front Microbiol *10*, 630. 10.3389/fmicb.2019.00630.

19. Plataki, M., Cho, S.J., Harris, R.M., Huang, H.R., Yun, H.S., Schiffer, K.T., and Stout-Delgado, H.W. (2019). Mitochondrial Dysfunction in Aged Macrophages and Lung during Primary Streptococcus pneumoniae Infection is Improved with Pirfenidone. Sci Rep *9*, 971. 10.1038/s41598-018-37438-1.

20. Chun, Y.Y., Tan, K.S., Yu, L., Pang, M., Wong, M.H.M., Nakamoto, R., Chua, W.Z., Huee-Ping Wong, A., Lew, Z.Z.R., Ong, H.H., et al. (2023). Influence of glycan structure on the colonization of Streptococcus pneumoniae on human respiratory epithelial cells. Proc Natl Acad Sci U S A *120*, e2213584120. 10.1073/pnas.2213584120.

21. Surabhi, S., Jachmann, L.H., Shumba, P., Burchhardt, G., Hammerschmidt, S., and Siemens, N. (2022). Hydrogen Peroxide Is Crucial for NLRP3 Inflammasome-Mediated IL-1beta Production and Cell Death in Pneumococcal Infections of Bronchial Epithelial Cells. J Innate Immun *14*, 192-206. 10.1159/000517855.

22. Brissac, T., Shenoy, A.T., Patterson, L.A., and Orihuela, C.J. (2018). Cell Invasion and Pyruvate Oxidase-Derived H(2)O(2) Are Critical for Streptococcus pneumoniae-Mediated Cardiomyocyte Killing. Infect Immun *86*. 10.1128/IAI.00569-17.

23. Alibayov, B., Scasny, A., Vidal, A.G.J., Murin, L., Wong, S., Edwards, K.S., Eichembaun, Z., Punshon, T., Jackson, B.P., Hopp, M.T., et al. (2023). Oxidation of hemoglobin in the lung parenchyma facilitates the differentiation of pneumococci into encapsulated bacteria. bioRxiv. 10.1101/2023.11.14.567109.

24. Landino, L.M., Hagedorn, T.D., Kim, S.B., and Hogan, K.M. (2011). Inhibition of tubulin polymerization by hypochlorous acid and chloramines. Free Radic Biol Med *50*, 1000-1008. 10.1016/j.freeradbiomed.2011.01.018.

25. Clark, H.M., Hagedorn, T.D., and Landino, L.M. (2014). Hypothiocyanous acid oxidation of tubulin cysteines inhibits microtubule polymerization. Arch Biochem Biophys *541*, 67-73. 10.1016/j.abb.2013.10.026.

26. Goldblum, R.R., McClellan, M., White, K., Gonzalez, S.J., Thompson, B.R., Vang, H.X., Cohen, H., Higgins, L., Markowski, T.W., Yang, T.Y., et al. (2021). Oxidative stress pathogenically remodels the cardiac myocyte cytoskeleton via structural alterations to the microtubule lattice. Dev Cell *56*, 2252-2266 e2256. 10.1016/j.devcel.2021.07.004.

27. Vallelian, F., Pimenova, T., Pereira, C.P., Abraham, B., Mikolajczyk, M.G., Schoedon, G., Zenobi, R., Alayash, A.I., Buehler, P.W., and Schaer, D.J. (2008). The reaction of hydrogen peroxide with hemoglobin induces extensive alpha-globin crosslinking and impairs the interaction of hemoglobin with endogenous scavenger pathways. Free Radic Biol Med *45*, 1150-1158. 10.1016/j.freeradbiomed.2008.07.013.

28. Jia, Y., Buehler, P.W., Boykins, R.A., Venable, R.M., and Alayash, A.I. (2007). Structural basis of peroxide-mediated changes in human hemoglobin: a novel oxidative pathway. J Biol Chem *282*, 4894-4907. 10.1074/jbc.M609955200.

29. Osellame, L.D., Blacker, T.S., and Duchen, M.R. (2012). Cellular and molecular mechanisms of mitochondrial function. Best Pract Res Clin Endocrinol Metab *26*, 711-723. 10.1016/j.beem.2012.05.003.

30. Akram, M. (2014). Citric acid cycle and role of its intermediates in metabolism. Cell Biochem Biophys *68*, 475-478. 10.1007/s12013-013-9750-1.

31. Kim, H.J., Khalimonchuk, O., Smith, P.M., and Winge, D.R. (2012). Structure, function, and assembly of heme centers in mitochondrial respiratory complexes. Biochim Biophys Acta *1823*, 1604-1616. 10.1016/j.bbamcr.2012.04.008.

32. Schumacker, P.T., Gillespie, M.N., Nakahira, K., Choi, A.M., Crouser, E.D., Piantadosi, C.A., and Bhattacharya, J. (2014). Mitochondria in lung biology and pathology: more than just a powerhouse. Am J Physiol Lung Cell Mol Physiol *306*, L962-974. 10.1152/ajplung.00073.2014.

33. Sharma, L.K., Lu, J., and Bai, Y. (2009). Mitochondrial respiratory complex I: structure, function and implication in human diseases. Curr Med Chem *16*, 1266-1277. 10.2174/092986709787846578.

34. Alibayov, B., Scasny, A., Khan, F., Creel, A., Smith, P., Vidal, A.G.J., Fitisemanu, F.M., Padilla-Benavides, T., Weiser, J.N., and Vidal, J.E. (2022). Oxidative Reactions Catalyzed by Hydrogen Peroxide Produced by Streptococcus pneumoniae and Other Streptococci Cause the Release and Degradation of Heme from Hemoglobin. Infect Immun *90*, e0047122. 10.1128/iai.00471-22.

35. Lanie, J.A., Ng, W.L., Kazmierczak, K.M., Andrzejewski, T.M., Davidsen, T.M., Wayne, K.J., Tettelin, H., Glass, J.I., and Winkler, M.E. (2007). Genome sequence of Avery's virulent serotype 2 strain D39 of Streptococcus pneumoniae and comparison with that of unencapsulated laboratory strain R6. J Bacteriol *189*, 38-51. 10.1128/JB.01148-06.

36. Tettelin, H., Nelson, K.E., Paulsen, I.T., Eisen, J.A., Read, T.D., Peterson, S., Heidelberg, J., DeBoy, R.T., Haft, D.H., Dodson, R.J., et al. (2001). Complete genome sequence of a virulent isolate of Streptococcus pneumoniae. Science *293*, 498-506. 10.1126/science.1061217.

37. McDevitt, E., Khan, F., Scasny, A., Thompson, C.D., Eichenbaum, Z., McDaniel, L.S., and Vidal, J.E. (2020). Hydrogen Peroxide Production by Streptococcus pneumoniae

Results in Alpha-hemolysis by Oxidation of Oxy-hemoglobin to Met-hemoglobin. mSphere *5*. 10.1128/mSphere.01117-20.

38. Nagababu, E., and Rifkind, J.M. (2000). Heme degradation during autoxidation of oxyhemoglobin. Biochem Biophys Res Commun *273*, 839-845. 10.1006/bbrc.2000.3025.

39. Hulko, M., Hospach, I., Krasteva, N., and Nelles, G. (2011). Cytochrome c biosensor--a model for gas sensing. Sensors (Basel) *11*, 5968-5980. 10.3390/s110605968.

40. Koch, H.-G., Schneider, Dirk (2007). Folding, Assembly, and Stability of Transmembrane Cytochromes. Current Chemical Biology *1*, 59-74. DOI: 10.2174/187231307779814020.

41. Imlay, J.A., Chin, S.M., and Linn, S. (1988). Toxic DNA damage by hydrogen peroxide through the Fenton reaction in vivo and in vitro. Science *240*, 640-642. 10.1126/science.2834821.

42. Winterbourn, C.C. (1995). Toxicity of iron and hydrogen peroxide: the Fenton reaction. Toxicol Lett *82-83*, 969-974. 10.1016/0378-4274(95)03532-x.

43. Chen, Y.R., Chen, C.L., Chen, W., Zweier, J.L., Augusto, O., Radi, R., and Mason, R.P. (2004). Formation of protein tyrosine ortho-semiquinone radical and nitrotyrosine from cytochrome c-derived tyrosyl radical. J Biol Chem *279*, 18054-18062. 10.1074/jbc.M307706200.

44. Lawrence, A., Jones, C.M., Wardman, P., and Burkitt, M.J. (2003). Evidence for the role of a peroxidase compound I-type intermediate in the oxidation of glutathione, NADH, ascorbate, and dichlorofluorescin by cytochrome c/H2O2. Implications for oxidative stress during apoptosis. J Biol Chem *278*, 29410-29419. 10.1074/jbc.M300054200.

45. Youle, R.J., and van der Bliek, A.M. (2012). Mitochondrial fission, fusion, and stress. Science *337*, 1062-1065. 10.1126/science.1219855.

46. Gnaiger, E. (2020). Mitochondrial pathways and respiratory control: An Introduction to OXPHOS Analysis. 5th ed.

47. Zhu, Y., Chidekel, A., and Shaffer, T.H. (2010). Cultured human airway epithelial cells (calu-3): a model of human respiratory function, structure, and inflammatory responses. Crit Care Res Pract *2010*. 10.1155/2010/394578.

48. Klabunde, B., Wesener, A., Bertrams, W., Beinborn, I., Paczia, N., Surmann, K., Blankenburg, S., Wilhelm, J., Serrania, J., Knoops, K., et al. (2023). NAD(+) metabolism is a key modulator of bacterial respiratory epithelial infections. Nat Commun *14*, 5818. 10.1038/s41467-023-41372-w.

49. Zorova, L.D., Popkov, V.A., Plotnikov, E.Y., Silachev, D.N., Pevzner, I.B., Jankauskas, S.S., Babenko, V.A., Zorov, S.D., Balakireva, A.V., Juhaszova, M., et al. (2018). Mitochondrial membrane potential. Anal Biochem *552*, 50-59. 10.1016/j.ab.2017.07.009.

50. Kress, T.R., Sabo, A., and Amati, B. (2015). MYC: connecting selective transcriptional control to global RNA production. Nat Rev Cancer *15*, 593-607. 10.1038/nrc3984.

51. Titov, D.V., Cracan, V., Goodman, R.P., Peng, J., Grabarek, Z., and Mootha, V.K. (2016). Complementation of mitochondrial electron transport chain by manipulation of the NAD+/NADH ratio. Science *352*, 231-235. 10.1126/science.aad4017.

52. Weiser, J.N., Ferreira, D.M., and Paton, J.C. (2018). Streptococcus pneumoniae: transmission, colonization and invasion. Nat Rev Microbiol *16*, 355-367. 10.1038/s41579-018-0001-8.

53. DeBerardinis, R.J., and Chandel, N.S. (2020). We need to talk about the Warburg effect. Nat Metab *2*, 127-129. 10.1038/s42255-020-0172-2.

54. Mado, K., Chekulayev, V., Shevchuk, I., Puurand, M., Tepp, K., and Kaambre, T. (2019). On the role of tubulin, plectin, desmin, and vimentin in the regulation of mitochondrial energy fluxes in muscle cells. Am J Physiol Cell Physiol *316*, C657-C667. 10.1152/ajpcell.00303.2018.

55. Guzun, R., Karu-Varikmaa, M., Gonzalez-Granillo, M., Kuznetsov, A.V., Michel, L., Cottet-Rousselle, C., Saaremae, M., Kaambre, T., Metsis, M., Grimm, M., et al. (2011). Mitochondria-cytoskeleton interaction: distribution of beta-tubulins in cardiomyocytes and HL-1 cells. Biochim Biophys Acta *1807*, 458-469. 10.1016/j.bbabio.2011.01.010.

56. O'Brien, K.L., Bronsdon, M.A., Dagan, R., Yagupsky, P., Janco, J., Elliott, J., Whitney, C.G., Yang, Y.H., Robinson, L.G., Schwartz, B., and Carlone, G.M. (2001). Evaluation of a medium (STGG) for transport and optimal recovery of Streptococcus pneumoniae from nasopharyngeal secretions collected during field studies. J Clin Microbiol *39*, 1021-1024. 10.1128/JCM.39.3.1021-1024.2001.

57. Edwards, K.S., Ashraf, S., Lomax, T.M., Wiseman, J.M., Hall, M.E., Gava, F.N., Hall, J.E., Hosler, J.P., and Harmancey, R. (2018). Uncoupling protein 3 deficiency impairs myocardial fatty acid oxidation and contractile recovery following ischemia/reperfusion. Basic Res Cardiol *113*, 47. 10.1007/s00395-018-0707-9.

58. Shirey, K., Stover, K.R., Cleary, J., Hoang, N., and Hosler, J. (2016). Membrane-Anchored Cyclic Peptides as Effectors of Mitochondrial Oxidative Phosphorylation. Biochemistry *55*, 2100-2111. 10.1021/acs.biochem.5b01368.

59. Makrecka-Kuka, M., Krumschnabel, G., and Gnaiger, E. (2015). High-Resolution Respirometry for Simultaneous Measurement of Oxygen and Hydrogen Peroxide Fluxes in Permeabilized Cells, Tissue Homogenate and Isolated Mitochondria. Biomolecules *5*, 1319-1338. 10.3390/biom5031319.

60. Tretter, L., and Ambrus, A. (2014). Measurement of ROS homeostasis in isolated mitochondria. Methods Enzymol *547*, 199-223. 10.1016/B978-0-12-801415-8.00012-6.

61. Han, S., Lee, M., Shin, Y., Giovanni, R., Chakrabarty, R.P., Herrerias, M.M., Dada, L.A., Flozak, A.S., Reyfman, P.A., Khuder, B., et al. (2023). Mitochondrial integrated stress response controls lung epithelial cell fate. Nature *620*, 890-897. 10.1038/s41586-023-06423-8.

Figure legends

Figure 1. Spn-H_2O_2 induces cytochrome c oxidation and tyrosyl radical formation. (A-F) Spn strains were incubated in THY-Cyt*c* medium at 37C with 5%CO_2. At the indicated time (A, C) or 6 h post-inoculation (B, D, E, F), supernatants were analyzed by spectroscopy. Controls included mock-infected medium (Cyt*c*), or TIGR4 and EF3030 supplemented with 500 U catalase. Panels (A, C) show 405 nm absorbance, (B, D) show Soret peak absorbance, and panels (E, F) display α and β peak absorbance. Statistical significance was assessed using one-way ANOVA with Dunnett's post hoc test (A, C) or Student's t-test (B, D). Significance levels: NS, not significant; *$p < 0.05$; **$p < 0.001$; ***$p < 0.0005$; ****$p < 0.0001$. (G) For spin-trapping, supernatants from Spn strains cultured for 4 h in THY medium were used. Cytochrome c (Cytc, 56 µM) and DEPMPO (30 mM) were added to supernatants to a final volume of 40 µL. Spectra (-Cyt*c*, black; +Cyt*c*, red) represent an average of 20 scans,

corrected for buffer baseline. Uninfected THY medium served as a control (ctrl). Spn-H_2O_2-free samples (+Cat) were prepared by pretreating supernatants with catalase for 1 min.

Figure 2. Spn-H_2O_2 modifies mitochondrial morphology, induces aggregation, and promotes mislocalization. Human alveolar A549 cells were either mock-infected or infected with Spn strains and incubated for 8 h at 37°C with 5% CO_2. Infected cells were stained for mitochondria (green), DNA (blue), and actin (red), imaged via confocal microscopy, and analyzed using Imaris software. Panels (A and B) display XY optical-middle sections (0.5 µm) from z-stacks. Panel (B) additionally includes XY, XZ (bottom), and YZ (side) optical sections. Three-dimensional reconstructions were generated from z-stacks, with panel (C) presenting simultaneous XY and XZ optical sections. Arrows in panels (A-C) indicate aggregated mitochondria. Confocal microscopy images are representative of at least three independent experiments. (D-F) Imaris software was employed to generate masks from the mitochondrial channel, enabling the assessment of subcellular localization (apical, middle, or basal) and quantification of mitochondrial area (µm²). Panel (D) depicts cells infected with strain EF3030, with the top panel showing all z-stacks, highlighting predominant apical mislocalization of mitochondria, and the bottom panel a middle optical section. Panel (E) presents three-dimensional images across all conditions as in (D), while panel (F) quantifies mitochondrial area under each infection condition. Data are expressed as mean ± SEM from confocal micrographs of three independent experiments. Statistical significance was assessed using one-way ANOVA with Dunnett's post hoc test, and **** indicating $p < 0.0001$.

Figure 3. Selective inhibition of complex-I driven respiration by Spn-H_2O_2. (A) H_2O_2 concentrations in supernatants from Spn cultured in THY medium (37°C, 4 h) were quantified using Amplex Red assay (LOD<0.56 µM). Data represent mean ± SEM; unpaired Student's t-

test, ****p < 0.0001. (B) Schematic of the mitochondrial ETC in lung epithelial cells[61]. (C-E) Heart mitochondria were treated with filter-sterilized Spn culture supernatants from Spn strains collected after 4 h of growth. (C) Complex I-driven respiration (CIDR) and (D) Complex II-driven respiration (CIIDR) were measured via Oroboros O2K FluoRespirometry. (E) Residual Complex I and II enzymatic activities relative to mock-treated controls. Data represent mean ± SEM; (C, D) unpaired Student's t-test, *p < 0.05 versus mock; (E) one-way ANOVA with Dunnett's post hoc test, ns, not significant; *p < 0.05; **p < 0.005; ****p < 0.0001. Complex I-driven respiration (CIDR) (C and E) or Complex II-driven respiration (CIDR) (D) was measured in an Oroboros O2K FluoRespirometer. Statistical analysis, (C and D) Student's t-test, *, *p*<0.05 compared against mock-treated heart mitochondria and or one-way ANOVA with Dunnet's test for multiple comparisons (I, K). ns, not significant; *, p < 0.05; ***, p < 0.005; **, p < 0.0001. (F) Complex I activity in mitochondria treated with Spn supernatants (~50 µM H_2O_2) or mock-treated, measured as NADH oxidation rate, normalized to protein content. Data represent mean ± SEM; unpaired Student's t-test, ****p < 0.0001.

Figure 4. S. pneumoniae-derived H_2O_2 inhibits TCA cycle enzymes and mitochondrial respiration. (A) Diagram of the canonical tricarboxylic acid (TCA) cycle, highlighting enzymes and electron donors (NADH, $FADH_2$). ETF, electron-transferring flavoprotein complex; α-KG, alpha-ketoglutarate. (B, C) Heart mitochondria were mock-treated or treated with filter-sterilized Spn culture supernatants (~50 µM H_2O_2, collected after 4 h growth). (B) Complex I-driven respiration (CIDR) and Complex II-driven respiration (CIIDR) were measured using Oroboros O2K FluoRespirometry with substrates: (CIDR) 10 mM pyruvate, 5 mM malate, 2 mM ADP, or 20 mM glutamate, 5 mM malate, 2 mM ADP; (CIIDR) 20 mM succinate, 2 mM ADP. (C) CIDR was measured with fatty acid substrates oleate and octanoate. (D–F)

Enzymatic activities of aconitase, glutamate dehydrogenase (GDH), and α-ketoglutarate dehydrogenase were measured in heart mitochondria mock-treated or treated with Spn supernatants (~50 μM H_2O_2), as described in Materials and Methods. (G) GDH activity was assessed in Calu-3 lung epithelial cells infected with Spn strains. (H, I) RNA-seq analysis of human bronchial Calu-3 cells mock-infected or infected with Spn strains. Heatmaps depict expression of (H) mitochondria-related or (I) oxidative stress-related genes. (B–G) Data represent mean ± SEM; one-way ANOVA with Dunnett's post hoc test, ns, not significant; *p < 0.05; **p < 0.005; ***p < 0.0005; ****p < 0.0001.

Figure 5. Spn-H_2O_2 drives Warburg-like metabolic reprogramming in lung epithelial cells. (A–C, E–G) Human bronchial Calu-3 cells were mock-infected, infected with Spn strains, or incubated with Spn cultured in cell culture medium for 8 h. Culture supernatants (extracellular) or cell pellets (intracellular) were harvested to quantify levels of (A, B) citrate, (C) glucose, (E) acetate, and (F, G) lactate, as described in Materials and Methods. Data represent mean ± SEM; one-way ANOVA with Dunnett's post hoc test (versus mock-infected cells) or unpaired Student's t-test (versus TIGR4 strain); ns, not significant; *p < 0.05; **p < 0.005; ***p < 0.0005; ****p < 0.0001. (D) Diagram of pyruvate node reactions under aerobic conditions, incorporating oxaloacetate and citrate. Enzymes are highlighted in gray. (H) RNA-seq analysis of Calu-3 cells mock-infected or infected with Spn strains. Heatmap depicts expression of glycolysis-related genes. (I) Schematic of the canonical glycolysis pathway, highlighting genes encoding enzymes upregulated in RNA-seq analysis.

Figure 6. *Streptococcus pneumoniae*-derived H_2O_2 does not significantly alter mitochondrial membrane potential in lung epithelial cells. (A–H) Human alveolar A549 cells were mock-treated, treated with CCCP, H2O2, EF3030, EF3030Δ*spxB*Δ*lctO* or EF3030

and CCCP for 10 h. Cells were stained with JC-1 dye for flow cytometric analysis and counterstained with SYTOX Blue to exclude dead cells. (A–F) Scatter plots showing JC-1 fluorescence (TexasRed/FITC) for each condition, with gating to identify live cells. (G and I) Quantification of change in mitochondrial membrane potential (Δψm) or (H and F) percent of live cells expressed as mean ± SEM from three independent experiment; one-way ANOVA with Dunnett's post hoc test; ns, not significant; *p < 0.05; **p < 0.01; ****p < 0.0001.

Figure 7. Limited contribution of Spn-H_2O_2 to apoptosis in lung epithelial cells. (A) Human alveolar A549 cells were mock-infected, treated with DNaseI (1U), treated with H_2O_2 (2 mM) added every 2 h, infected with TIGR4, TIGR4Δ*spxB*Δ*lctO*, EF3030, EF3030Δ*spxB*Δ*lctO* or EF3030 for 8 h. Cells were stained with the Click-iT Plus TUNEL assay kit, and mounted on slides with DAPI-containing resin and analyzed by confocal microscopy using the Imaris software. (B-C) Fluorescence intensity (FITC/GFP) from each condition, reported as arbitrary units (AU), quantifying TUNEL staining. (D, E) RNA-seq analysis of Calu-3 (D) or BEAS-2B (E) cells mock-infected or infected with Spn strains. Heatmaps depict expression of mitochondria-related and apoptosis-related genes. (B–C) Data represent mean ± SEM from two independent experiments with four internal replicates each; one-way ANOVA with Dunnett's post hoc test; ns, not significant; *p < 0.05; **p < 0.01; ****p < 0.0001. (G) Heatmap visualization compares gene expression levels. Genes analyzed include those encoding pyruvate node enzymes, pneumolysin (ply) and capsule locus genes

Graphical abstract

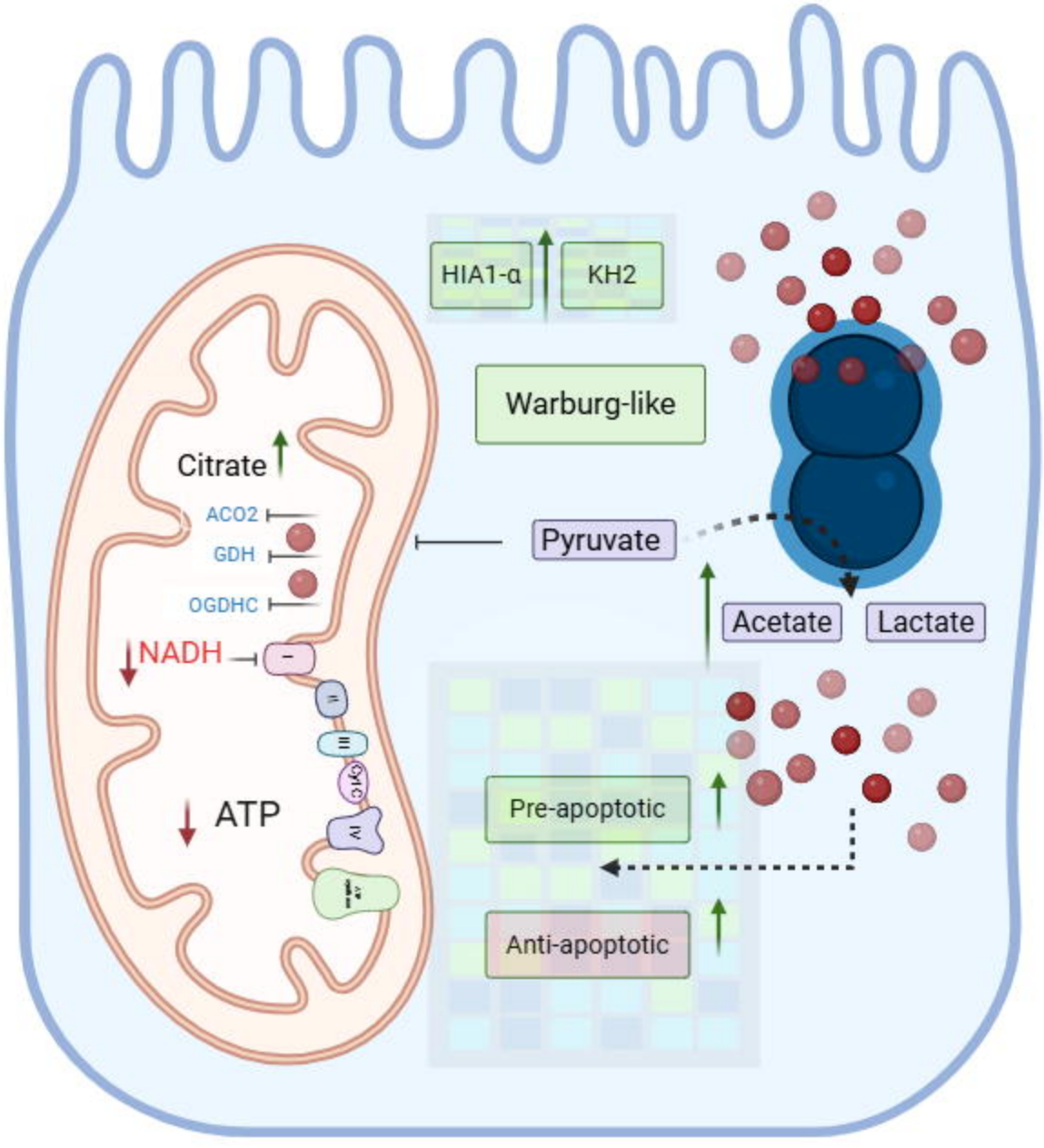

Figure 1

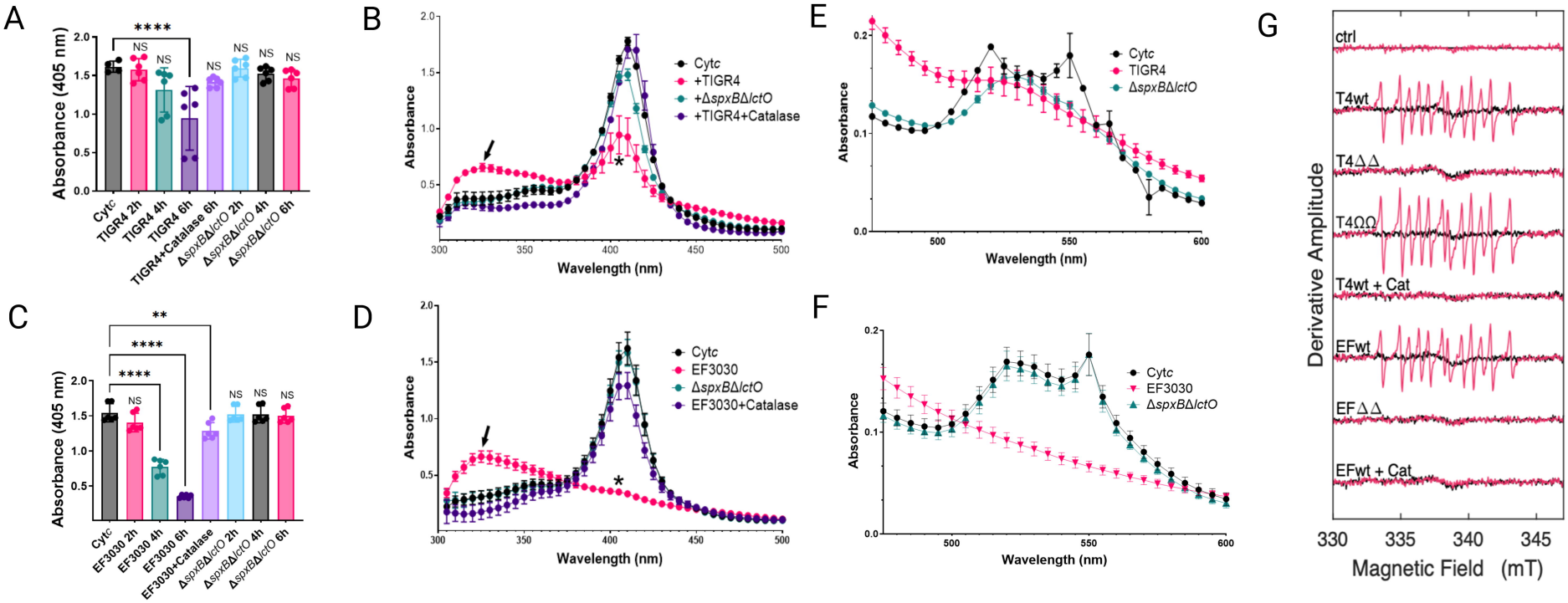
A
Absorbance (405 nm)
****
NS
Cytc
TIGR4 2h
TIGR4 4h
TIGR4 6h
TIGR4+Catalase 6h
ΔspxBΔlctO 2h
ΔspxBΔlctO 4h
ΔspxBΔlctO 6h
B
Absorbance
Wavelength (nm)
Cytc
+TIGR4
+ΔspxBΔlctO
+TIGR4+Catalase
C
Absorbance (405 nm)
**
****
EF3030 2h
EF3030 4h
EF3030 6h
EF3030+Catalase
D
EF3030
EF3030+Catalase
E
F
G
ctrl
T4wt
T4ΔΔ
T4ΩΩ
T4wt + Cat
EFwt
EFΔΔ
EFwt + Cat
Derivative Amplitude
Magnetic Field (mT)

Figure 2

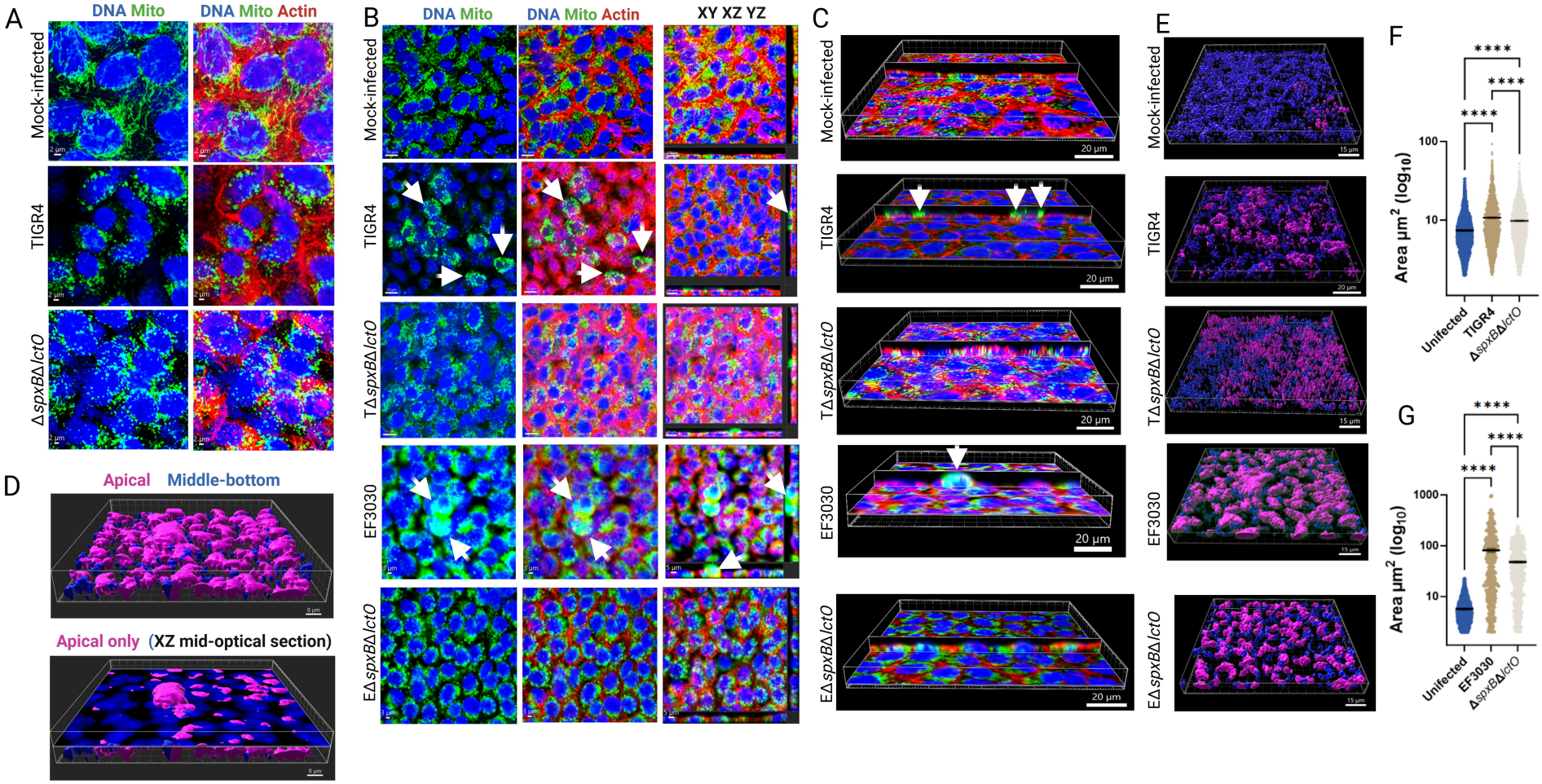
A
DNA Mito
DNA Mito Actin
Mock-infected
TIGR4
ΔspxBΔlctO
B
DNA Mito
DNA Mito Actin
XY XZ YZ
Mock-infected
TIGR4
TΔspxBΔlctO
EF3030
EΔspxBΔlctO
C
Mock-infected
TIGR4
TΔspxBΔlctO
EF3030
EΔspxBΔlctO
20 µm
E
Mock-infected
TIGR4
TΔspxBΔlctO
EF3030
EΔspxBΔlctO
D
Apical
Middle-bottom
Apical only
(XZ mid-optical section)
F
Area µm² (log10)
Unifected
TIGR4
ΔspxBΔlctO
G
Area µm² (log10)
Unifected
EF3030
ΔspxBΔlctO

Figure 3

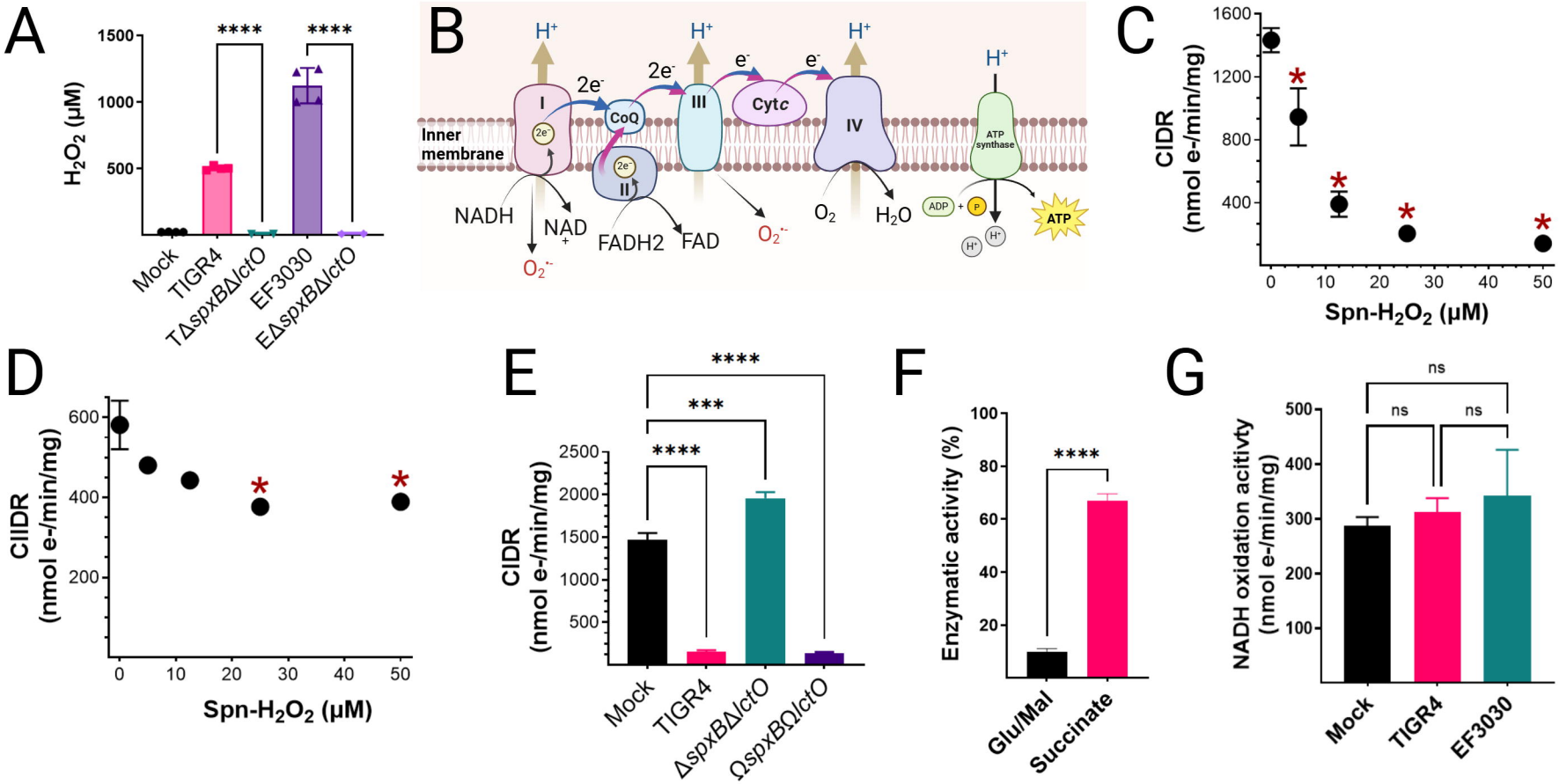
A
H_2O_2 (μM)
1500
1000
500
****
****
Mock
TIGR4
TΔspxBΔlctO
EF3030
EΔspxBΔlctO
B
H+
2e-
CoQ
I
II
III
IV
Cytc
e-
Inner membrane
NADH
NAD+
FADH2
FAD
$O_2^{\bullet-}$
O_2
H_2O
ADP
P
ATP synthase
ATP
C
CIDR (nmol e-/min/mg)
1600
1200
800
400
Spn-H_2O_2 (μM)
D
CIIDR (nmol e-/min/mg)
600
400
200
Spn-H_2O_2 (μM)
E
CIDR (nmol e-/min/mg)
2500
2000
1500
1000
500
****
***
****
Mock
TIGR4
ΔspxBΔlctO
ΩspxBΩlctO
F
Enzymatic activity (%)
100
80
60
40
20
****
Glu/Mal
Succinate
G
NADH oxidation acitivty (nmol e-/min/mg)
500
400
300
200
100
ns
ns
ns
Mock
TIGR4
EF3030

Figure 4

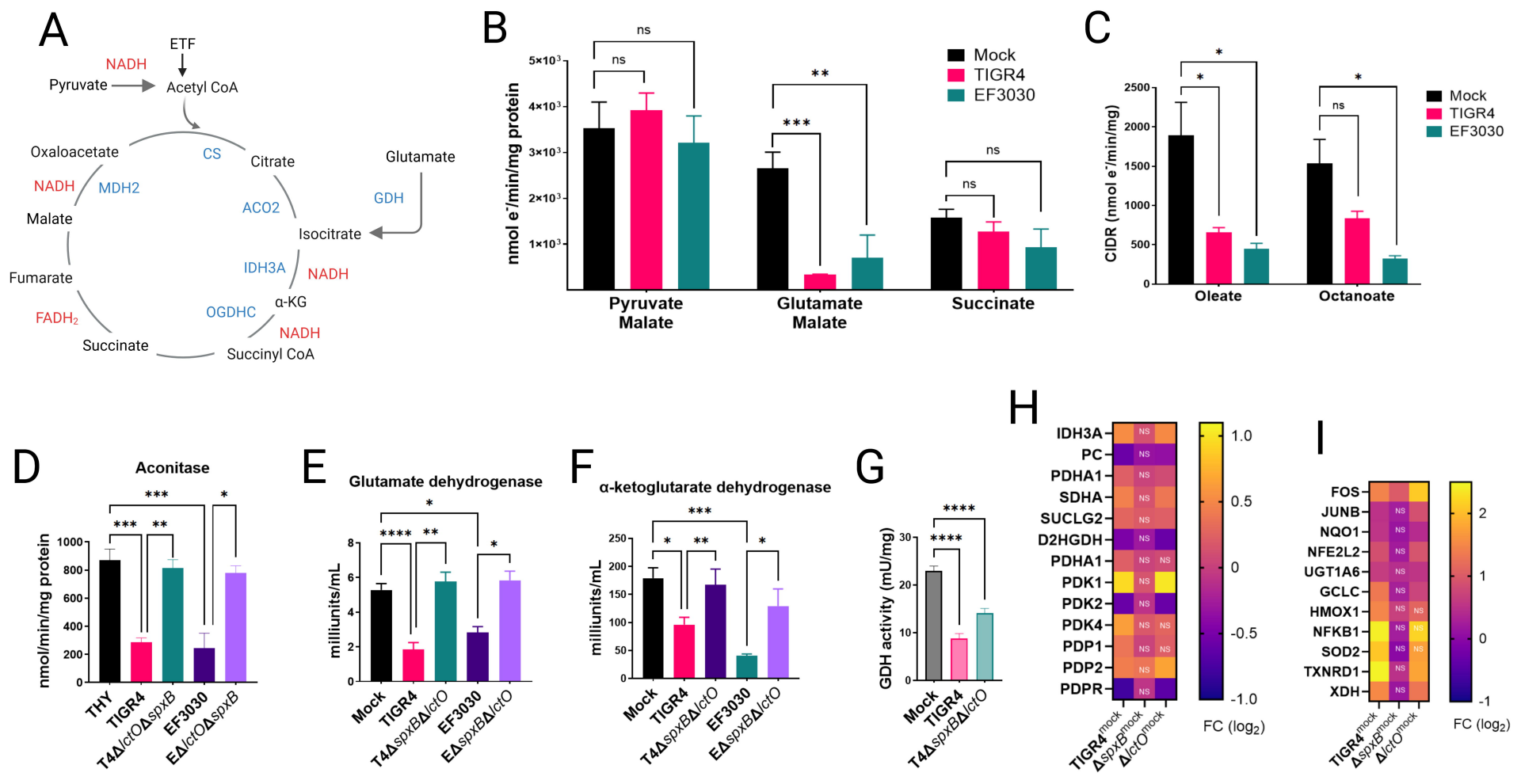
A
ETF
NADH
Pyruvate
Acetyl CoA
Oxaloacetate
CS
Citrate
Glutamate
NADH
MDH2
GDH
ACO2
Malate
Isocitrate
IDH3A
NADH
Fumarate
α-KG
OGDHC
FADH2
NADH
Succinate
Succinyl CoA
B
nmol e⁻/min/mg protein
Mock
TIGR4
EF3030
ns
ns
**
***
ns
ns
Pyruvate Malate
Glutamate Malate
Succinate
C
CIDR (nmol e⁻/min/mg)
Mock
TIGR4
EF3030
*
*
*
ns
Oleate
Octanoate
D
Aconitase
nmol/min/mg protein
THY
TIGR4
T4ΔlctOΔspxB
EF3030
EΔlctOΔspxB
E
Glutamate dehydrogenase
milliunits/mL
Mock
TIGR4
T4ΔspxBΔlctO
EF3030
EΔspxBΔlctO
F
α-ketoglutarate dehydrogenase
milliunits/mL
Mock
TIGR4
T4ΔspxBΔlctO
EF3030
EΔspxBΔlctO
G
GDH activity (mU/mg)
Mock
TIGR4
T4ΔspxBΔlctO
H
IDH3A
PC
PDHA1
SDHA
SUCLG2
D2HGDH
PDHA1
PDK1
PDK2
PDK4
PDP1
PDP2
PDPR
TIGR4mock
ΔspxBmock
ΔlctOmock
FC (log2)
I
FOS
JUNB
NQO1
NFE2L2
UGT1A6
GCLC
HMOX1
NFKB1
SOD2
TXNRD1
XDH
TIGR4mock
ΔspxBmock
ΔlctOmock
FC (log2)

Figure 5

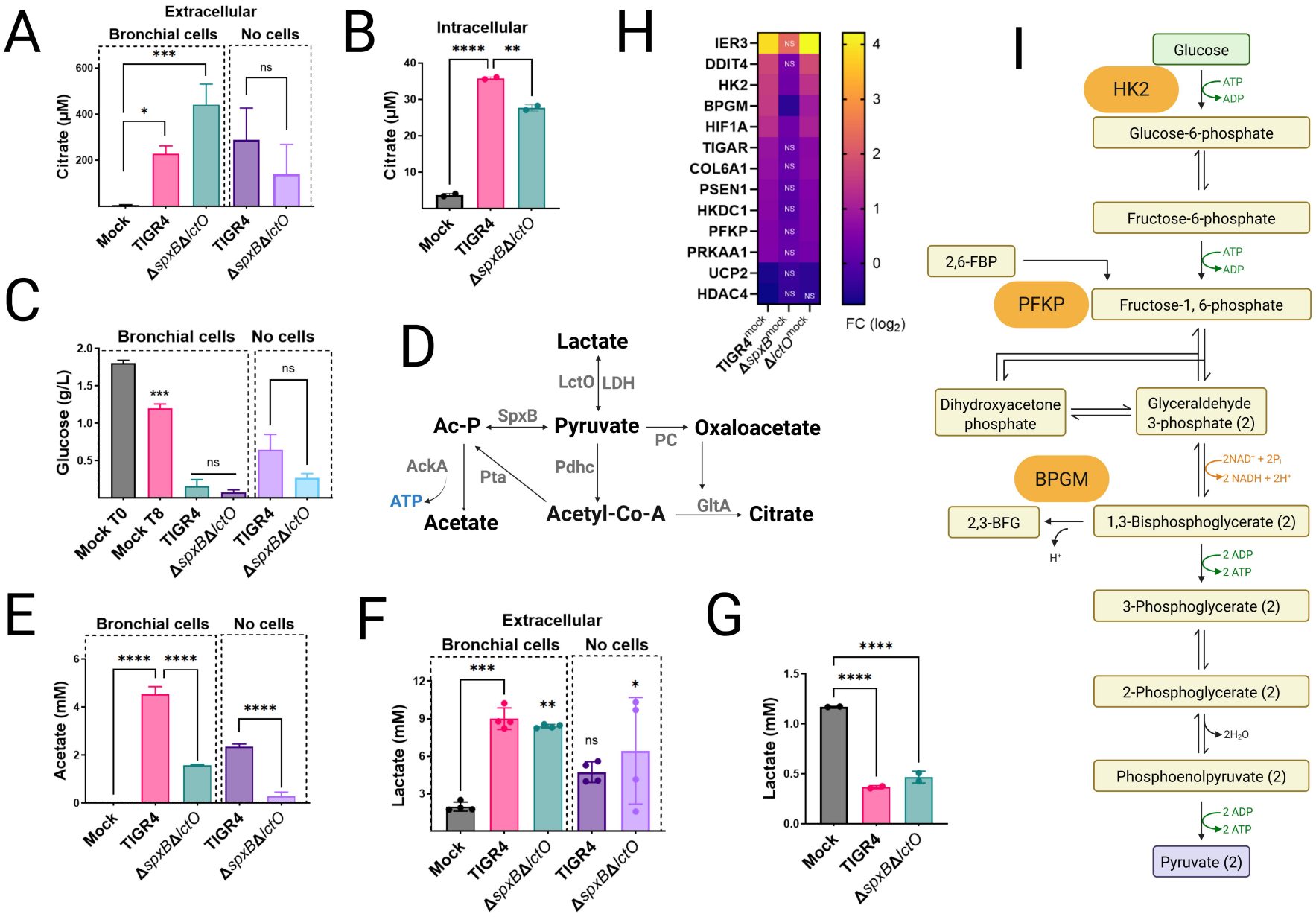
A
Extracellular
Bronchial cells
No cells
Citrate (µM)
Mock
TIGR4
ΔspxBΔlctO
B
Intracellular
Citrate (µM)
C
Bronchial cells
No cells
Glucose (g/L)
Mock T0
Mock T8
D
Lactate
LctO
LDH
Ac-P
SpxB
Pyruvate
PC
Oxaloacetate
AckA
ATP
Pta
Pdhc
Acetate
Acetyl-Co-A
GltA
Citrate
E
Bronchial cells
No cells
Acetate (mM)
F
Extracellular
Bronchial cells
No cells
Lactate (mM)
G
Lactate (mM)
H
IER3
DDIT4
HK2
BPGM
HIF1A
TIGAR
COL6A1
PSEN1
HKDC1
PFKP
PRKAA1
UCP2
HDAC4
FC (log2)
I
Glucose
HK2
ATP
ADP
Glucose-6-phosphate
Fructose-6-phosphate
2,6-FBP
PFKP
Fructose-1, 6-phosphate
Dihydroxyacetone phosphate
Glyceraldehyde 3-phosphate (2)
BPGM
2NAD+ + 2Pi
2 NADH + 2H+
2,3-BFG
1,3-Bisphosphoglycerate (2)
2 ADP
2 ATP
3-Phosphoglycerate (2)
2-Phosphoglycerate (2)
2H2O
Phosphoenolpyruvate (2)
Pyruvate (2)

Figure 6

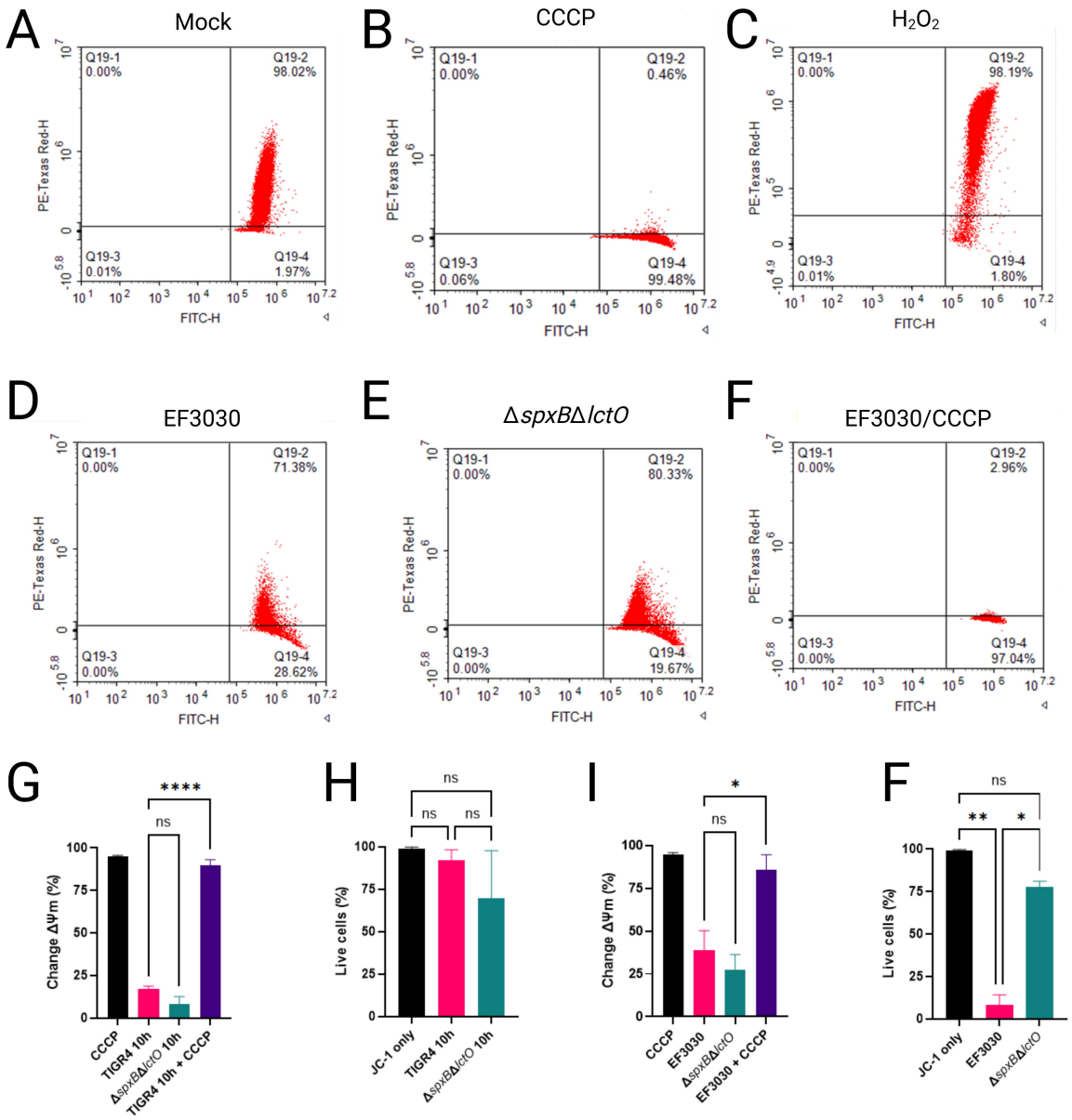
A
Mock
Q19-1 0.00%
Q19-2 98.02%
Q19-3 0.01%
Q19-4 1.97%
B
CCCP
Q19-1 0.00%
Q19-2 0.46%
Q19-3 0.06%
Q19-4 99.48%
C
H_2O_2
Q19-1 0.00%
Q19-2 98.19%
Q19-3 0.01%
Q19-4 1.80%
D
EF3030
Q19-1 0.00%
Q19-2 71.38%
Q19-3 0.00%
Q19-4 28.62%
E
ΔspxBΔlctO
Q19-1 0.00%
Q19-2 80.33%
Q19-3 0.00%
Q19-4 19.67%
F
EF3030/CCCP
Q19-1 0.00%
Q19-2 2.96%
Q19-3 0.00%
Q19-4 97.04%
PE-Texas Red-H
FITC-H
G
Change ΔΨm (%)
****
ns
CCCP
TIGR4 10h
ΔspxBΔlctO 10h
TIGR4 10h + CCCP
H
Live cells (%)
ns
ns
ns
JC-1 only
TIGR4 10h
ΔspxBΔlctO 10h
I
Change ΔΨm (%)
*
ns
CCCP
EF3030
ΔspxBΔlctO
EF3030 + CCCP
F
Live cells (%)
ns
**
*
JC-1 only
EF3030
ΔspxBΔlctO

Figure 7

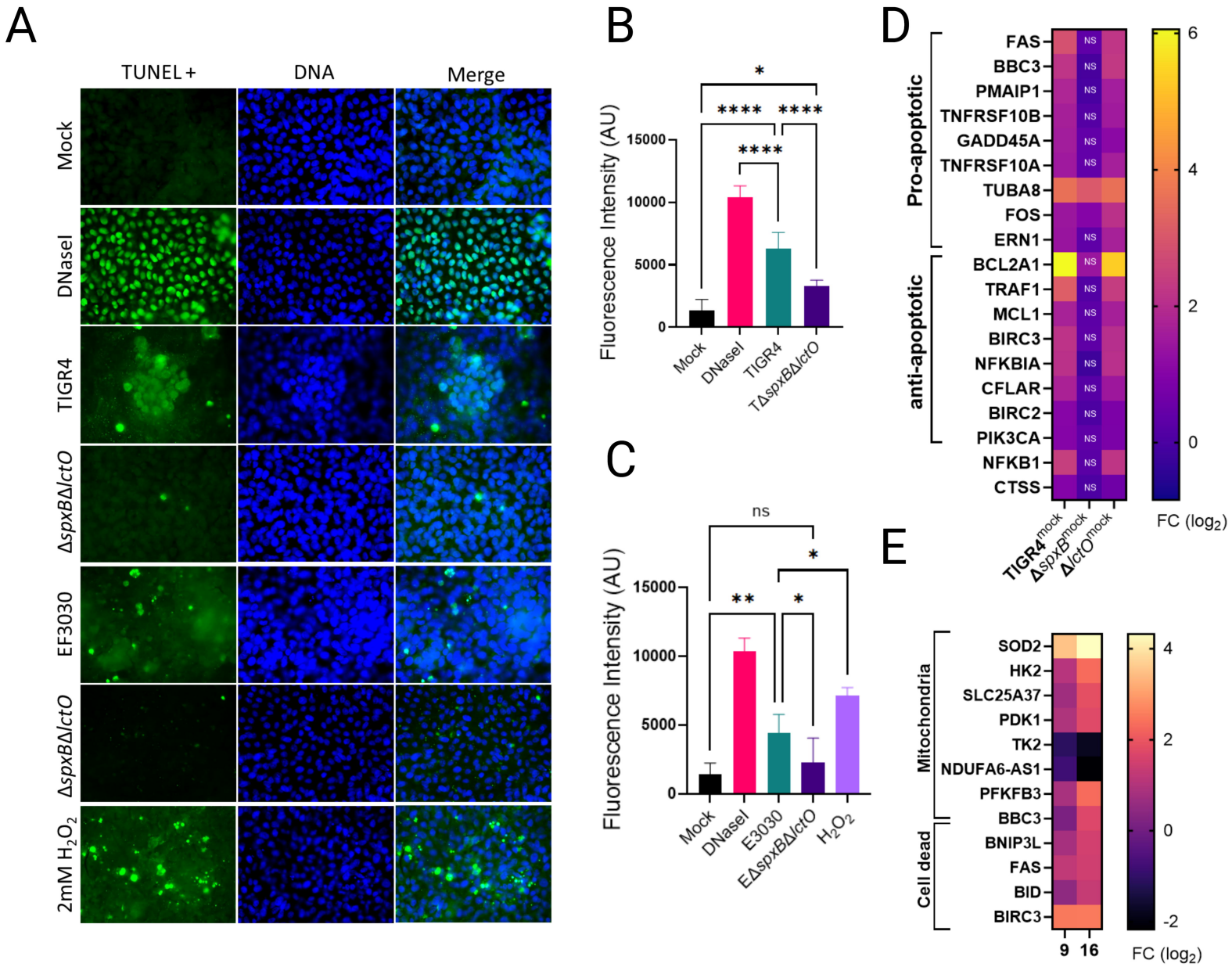
A
TUNEL+
DNA
Merge
Mock
DNaseI
TIGR4
ΔspxBΔlctO
EF3030
ΔspxBΔlctO
2mM H2O2
B
Fluorescence Intensity (AU)
15000
10000
5000
0
*
****
****
****
Mock
DNaseI
TIGR4
TΔspxBΔlctO
C
Fluorescence Intensity (AU)
15000
10000
5000
0
ns
*
**
*
Mock
DNaseI
E3030
EΔspxBΔlctO
H2O2
D
Pro-apoptotic
FAS
BBC3
PMAIP1
TNFRSF10B
GADD45A
TNFRSF10A
TUBA8
FOS
ERN1
anti-apoptotic
BCL2A1
TRAF1
MCL1
BIRC3
NFKBIA
CFLAR
BIRC2
PIK3CA
NFKB1
CTSS
NS
TIGR4mock
ΔspxBmock
ΔlctOmock
FC (log2)
6
4
2
0
E
Mitochondria
SOD2
HK2
SLC25A37
PDK1
TK2
NDUFA6-AS1
PFKFB3
Cell dead
BBC3
BNIP3L
FAS
BID
BIRC3
9
16
FC (log2)
4
2
0
-2